Journal of Energy

ISSN 1849–0751 (On–line)
ISSN 0013–7448 (Print)
UDK 621.31
https://doi.org/10.37798/EN2025743

VOLUME 74 Number 3 | 2025

74 ENERGIJA

Journal of Energy

Scientific Professional Journal Of Energy, Electricity, Power Systems
Online ISSN 1849–0751, Print ISSN 0013–7448, VOL 74
https://doi.org/10.37798/EN2024743

Published by
HEP d.d., Ulica grada Vukovara 37, HR–10000 Zagreb
HRO CIGRÉ, Berislavićeva 6, HR–10000 Zagreb
University of Zagreb FER, Unska 3, HR–10000 Zagreb

EDITORIAL

The first study, "A Novel Multi-Loop Base Carrier Mark PWM Strategy for Leakage Current Reduction in Grid-Connected Transformerless Inverters," presents a new multi-loop BCM pulse-width modulation strategy aimed at reducing leakage current in transformerless photovoltaic inverters. By combining sequential level shifting and single-, two-, and three-loop carrier rotation techniques, the approach significantly minimizes common-mode voltage variation and achieves strong leakage current suppression. Simulations confirm its effectiveness, with the STATE-V configuration reducing leakage current to just 2.021 mA, far below the 150 mA VDE 0126-1-1 limit. The study also outlines trade-offs between leakage reduction, THD, common-mode voltage stability, and efficiency across eight BCM configurations, offering a major advancement for safer and more reliable transformerless inverter systems and opening pathways for adaptive and AI-driven modulation methods.

The second article, "An Economy Aspect of Different Nuclear Energy Development," examines the economic and environmental significance of nuclear energy in meeting global electricity demand and addressing climate change. The authors analyze three development scenarios and compare nuclear energy with fossil fuels and renewables, highlighting its cost-effectiveness, reliability, and low greenhouse gas emissions. By evaluating long-term projections and levelized cost of electricity, the study underscores nuclear energy's role in reducing dependence on fossil fuels and advancing global climate goals, contributing important insights to discussions on sustainable energy transitions.

The article "Benchmark Calculation of FHR Fuel Assembly Phase I-C Depletion Exercises" presents initial results of Phase I-C depletion studies for the FHR physics benchmark. Advancing earlier OECD benchmarks, the work shifts from a pseudo-2D to a full 3D model of a single FHR fuel assembly containing TRISO fuel, graphite moderator, and FLiBe coolant. Using Serpent 2 and ENDF/B libraries, the authors evaluate keff, recoverable energy per fission, fission density rate, and axial offset up to 70 GWd/tU, showing the strong influence of cross-section libraries, xenon modeling, and depletion step size. The findings highlight the need for standardized guidelines and demonstrate the capability of Serpent 2 to model complex geometries and advanced reactor materials.

The article "Verification of the IRIS Numerical Model for the Severe Accident Calculation" provides an in-depth study of the IRIS small modular PWR and its safety-by-design features. The authors develop and couple RELAP5, GOTHIC, and ASYST codes to simulate severe accident and LOCA scenarios, emphasizing the reactor's integral configuration, passive safety systems, and high-pressure containment. Results show the effectiveness of these passive features in preserving core integrity and preventing overheating during design-basis accidents. The study offers valuable insights into advanced SMR safety behavior and highlights the importance of detailed numerical modeling in modern reactor design.

Igor Kuzle
Editor–in–Chief

Journal of Energy

VOLUME 74 Number 3 | 2025

journal homepage: http://journalofenergy.com/

A Novel Multi-Loop Base Carrier Mark PWM Strategy for Leakage Current Reduction in Grid-Connected Transformerless Inverters

Rajiya Begum Sayyad, Upendar Jalla

Summary — This paper presents a novel multi-loop Base Carrier Mark (BCM) pulse-width modulation strategy to address leakage current challenges in gridconnected transformerless photovoltaic inverters. The proposed approach introduces a combination of sequential level shift, single-loop, two-loop, and three-loop carrier rotation techniques in BCM generation, specifically designed to minimize common-mode voltage variations and suppress leakage current. The method's effectiveness was validated through comprehensive simulation studies using Matlab/Simulink, evaluating eight distinct BCM configurations. Results demonstrate that the proposed multi-loop BCM strategy, particularly in STATE-V configuration, achieves superior leakage current suppression while maintaining high system performance. This configuration reduces leakage current to 2.021 mA, significantly below the VDE 0126-1-1 standard limit of 150 mA (for 40ms fault discontinuity) and the conservative design threshold of 300 mA, without compromising other performance metrics. This configuration reduces leakage current significantly below the standard 300mA limit without compromising other performance metrics. The strategy also demonstrates favorable outcomes in Total Harmonic Distortion (THD < 2% in STATE-II & IV), common mode voltage stability (optimal in STATE-III), and system efficiency (peak performance in STATE-IV). These findings present a significant advancement in transformerless inverter technology, offering a practical solution to the critical challenge of leakage current in grid-connected PV systems. .

Keywords **— Carrier-Based Pulse-width modulation, Transformer-less PV inverter, Total Harmonic**

I. Introduction

The global energy landscape faces significant challenges amid the ongoing pandemic and geopolitical tensions, yet the renewable energy sector, particularly photovoltaics, continues to demonstrate remarkable resilience and growth [1]. This expansion is particularly crucial as the sharp rise in energy prices and geopolitical conflicts, such as the invasion of Ukraine by the Russian Federation, raise serious concerns about energy poverty affecting billions of people. In this context, renewable energy sources, especially photovoltaic and wind technology, must be prioritized to ensure energy security and continuity [2],[3].

Photovoltaic (PV) power systems have emerged as versatile solutions, comprising PV modules and power electronics converters as their fundamental components. These systems can operate in both off-grid and gridconnected configurations, requiring inverters to convert direct current (DC) to alternating current (AC) power [4], [5]. The selection between transformer-based and transformerless inverter topologies presents significant tradeoffs. While transformer-based structures offer galvanic isolation that enhances safety and reliability, they suffer from reduced efficiency and increased system volume, weight, and cost. Conversely, transformerless inverters, despite their advantages, face the critical challenge of leakage current (i_{CM}), which can compromise system safety and reliability [6].

Leakage current poses several significant challenges in transformerless PV systems, including grid current disruption, electromagnetic interference, and corrosion effects on PV panels [7]. Recent research by Yikun Wang (2024) has introduced innovative approaches for minimizing leakage current in three-phase transformerless PV inverters, demonstrating the ongoing efforts to address these challenges [8]. Additionally, studies have proposed advanced suppression methods for single-phase photovoltaic inverters, contributing to the growing body of solutions in this field [9].

In this study, we propose and evaluate multiple PWM techniques based on modified base carrier signals (BCM) for application in a grid-connected single-phase H6-IMPR type transformerless inverter [10]. Our investigation focuses on testing modified sequential level shift, single, two, and three-loop carrier rotation, carrier phase shift, and their derived PWM techniques. The proposed approaches aim to optimize system performance while effectively managing leakage current issues.

The remainder of this paper is organized as follows: Section 2 presents Related Research and Current Developments, section 3 gives a detailed discussion of the H6IMPR transformerless inverter's operating principles, the proposed BCM-based modulation techniques, system design considerations, and leakage current analysis. Section 4 provides comprehensive simulation results validating the effectiveness of the proposed modified BCM-based PWM techniques. Finally, Section 5 concludes the paper with key findings and recommendations for future research directions.

Corresponding author: Rajiya Begum Sayyad
Osmania University University College of Engineering, Osmania University
Rajiya Begum Sayyad and Upendar Jalla are with the Osmania University, Hyderabad, India (emails: rajiya.sd9@gmail.com; jallupendar@gmail.com).

Rajiya Begum Sayyad, Upendar Jalla, A Novel Multi-Loop Base Carrier Mark PWM Strategy for Leakage Current Reduction in Grid-Connected Transformerless Inverters, Journal of Energy, vol. 74 Number 3 (2025), 3–11
https://doi.org/10.37798/2025743722

II. Related Research and Current Developments

A. Topological Innovations

Recent advances in inverter topology design have yielded significant improvements in leakage current management. Tingrui Mao et al. (2024) introduced a novel solution based on active zero-sequence current injections for transformerless grid-connected PV converters, demonstrating enhanced leakage current suppression capabilities [11]. This work builds upon earlier research by Caique et al. (2023), who proposed innovative level modulation switching techniques for leakage current mitigation in transformerless grid-connected PV inverters [3].

B. Modulation Techniques and Control Strategies

The evolution of pulse-width modulation (PWM) techniques has significantly advanced transformerless inverter performance. Christopher Rodríguez-Cortés et al. (2023) provided a comprehensive overview of leakage current reduction methods in single-phase grid-connected inverters, highlighting the importance of advanced modulation strategies [12]. Geye Lu et al. (2023) further contributed to this field by developing an improved leakage-current-based online monitoring method, incorporating asymmetric voltage injection at photovoltaic inverter switching frequencies [13].

Recent developments in PWM techniques have demonstrated promising results in improving system performance. The implementation of improved large midspace vector modulation (ILMSVM) and commonmode subtraction space vector pulse-width modulation (CSSVPWM) has shown effectiveness in suppressing leakage current while enhancing other performance indicators such as total harmonic distortion [14]. Additionally, the Large Small Pulse Width Modulation (LS-PWM) technique has proven successful in reducing stress on both leakage current and switching elements in grid-connected single-phase five-level inverters [15].

C. Performance Enhancement Strategies

Significant progress has been made in developing comprehensive approaches to system optimization. Xiaolong Xiao et al. (2023) proposed innovative strategies for collecting and suppressing leakage current in non-isolated photovoltaic grid-connected systems, demonstrating the potential for improved system reliability [15]. Their work complements earlier research focusing on the development of hybrid/modified modulation techniques which have shown promising results in multilevel inverter applications [3], [12].

The implementation of modified sequential level-shifting PWM techniques in three-phase five-level inverters has demonstrated reduced stress on submodule capacitors [16]. Furthermore, alternative phase-countershifted PWM techniques applied to grid-connected single-phase halfimpedance source-based cascade five-level inverters have shown improved efficiency through various carrier rotation structures [10].

III. Methodology

A. H6-IMPR Inverter Topology and Operating Principles

The improved H6 (H6-IMPR) type transformerless inverter topology forms the foundation of this study [19]. This topology offers enhanced performance characteristics while maintaining fundamental inverter functionality. Fig. 1 illustrates the four basic operating states of the H6IMPR type inverter, showing the power exchange states and zero voltage states in both positive and negative halfcycles.

The inverter's operation can be categorized into four primary modes, each characterized by specific switch states and voltage parameters, as summarized in Table I. During the positive half-cycle (Mode 1), switches S1 and S4 conduct while S2, S3, S5, and S6 remain off, enabling power transfer from the photovoltaic (PV) modules to the grid.

Table I
H6-improved topology switch states S1 - S6.

$S1$	$S2$	$S3$	$S4$	$S5$	$S6$	$U_{\mathrm{an}}/\mathrm{V}$	$U_{\mathrm{bn}}/\mathrm{V}$	$U_{\mathrm{cm}}/\mathrm{V}$	$U_{\mathrm{ab}}/\mathrm{V}$	
1	0	0	1	0	0	U_{pv}	0	$U_{\mathrm{pv}}/2$	U_{pv}	P
0	0	0	0	0	1	$U_{\mathrm{pv}}/2$	$U_{\mathrm{pv}}/2$	$U_{\mathrm{pv}}/2$	0	
0	1	1	0	0	0	0	U_{pv}	$U_{\mathrm{pv}}/2$	$-U_{\mathrm{pv}}$	N
0	0	0	0	1	0	$U_{\mathrm{pv}}/2$	$U_{\mathrm{pv}}/2$	$U_{\mathrm{pv}}/2$	0	

In Mode 1, the voltage at point 'a' relative to neutral (U_{an}) equals the PV voltage (U_{PV}), while point 'b' maintains zero potential relative to neutral (U_{bn}). This results in a differential voltage (U_{ab}) of U_{PV} and a common-mode voltage (U_{cm}) of $0.5U_{PV}$.

B. Control Strategy and Modulation Technique

1) Overall Control Architecture: The proposed control strategy employs a cascaded control structure comprising inner current control loops and an outer voltage regulation loop, as illustrated in the enhanced block diagram of Fig. 4. This multi-loop architecture ensures both accurate current injection to the grid and stable DC-link voltage regulation under varying irradiance conditions.

The control system operates in the stationary α-β reference frame to minimize computational complexity while maintaining precise current tracking. A phase-locked loop (PLL) continuously monitors the grid voltage to extract critical synchronization parameters: grid frequency (f_g), angular frequency ($\omega_g = 2\pi f_g$), and phase angle (θ_g). These parameters ensure that the injected current maintains appropriate phase relationship with the grid voltage for desired active and reactive power control.

2) Reference Current Generation: The reference current (i^*_g) for the inner current control loop is synthesized through the following process:

1) The outer voltage controller compares the measured DC-link voltage (V_{pv}) with its reference value (V_{pv}^*) and processes the error through a PI controller:

$$I_{mag} = K_{p,v}(V_{pv}^* - V_{pv}) + K_{i,v}\int (V_{pv}^* - V_{pv})dt \quad (1)$$

where $K_{p,v} = 0.5$ and $K_{i,v} = 20$ are the proportional and integral gains of the voltage controller, tuned to achieve adequate bandwidth (approximately 10 Hz) while maintaining system stability with sufficient phase margin (> 45°).

2) The reference current waveform is constructed by multiplying I_{mag} with the normalized grid voltage template obtained from the PLL:

Rajiya Begum Sayyad, Upendar Jalla, A Novel Multi-Loop Base Carrier Mark PWM Strategy for Leakage Current Reduction in Grid-Connected Transformerless Inverters, Journal of Energy, vol. 74 Number 3 (2025), 3–11
https://doi.org/10.37798/2025743722

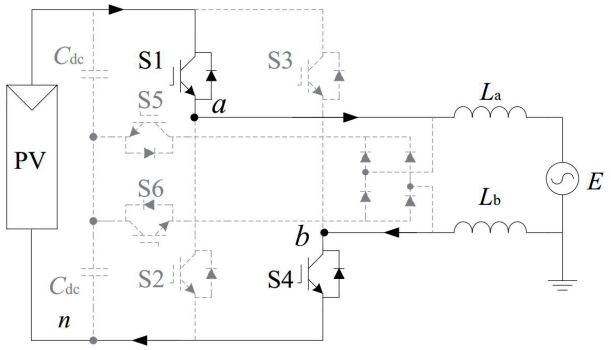

(a) Power exchange state in positive half-cycle

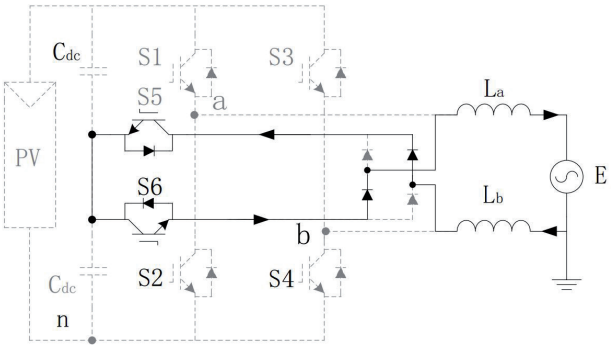

(b) Zero voltage state in positive half-cycle

$$i_g^*(t) = I_{mag} \cdot \sin(\omega_g t + \theta_g) \quad (2)$$

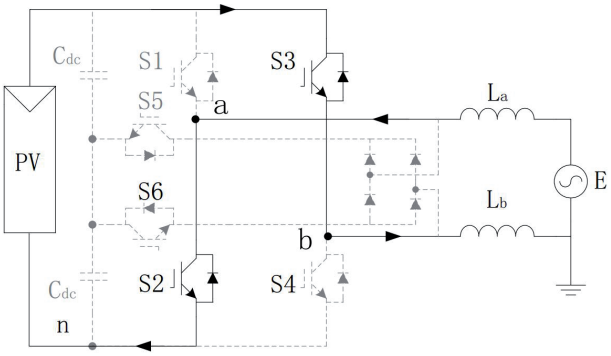

(c) Power exchange state in negative half-cycle

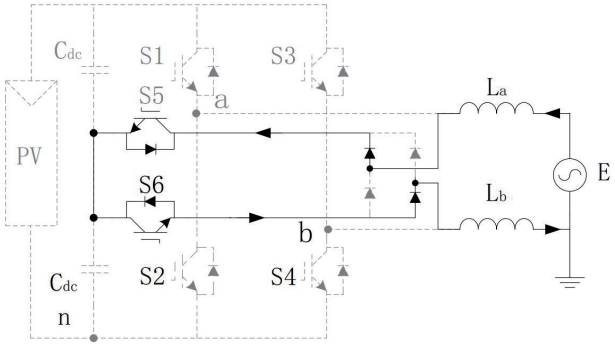

(d) Zero voltage state in negative half-cycle

Fig. 1. Improved H6 type inverter operating cases.

This approach ensures unity power factor operation (inphase current injection) while the magnitude automatically adjusts to balance power flow and maintain DC-link voltage stability.

3) *Inner Current Control Loop:* The inner current control loop regulates the actual grid current (i_g) to track the reference current (i^*_g) with high precision and fast dynamic response. A proportional-resonant (PR) controller is employed due to its superior capability in tracking sinusoidal references with zero steady-state error:

$$G_{PR}(s) = K_p + \frac{K_r s}{s^2 + \omega_0^2} \quad (3)$$

where $K_p = 10$ is the proportional gain, $K_r = 1000$ is the resonant gain, and $\omega_0 = 2\pi f_g = 314.16$ rad/s is the resonant frequency tuned to the grid frequency. The PR controller provides infinite gain at the fundamental frequency (50 Hz), ensuring zero tracking error for sinusoidal references while providing adequate attenuation of harmonic disturbances. The current loop bandwidth is designed to be approximately 1 kHz, providing fast dynamic response while remaining well below the switching frequency to avoid interaction with PWM harmonics.

The current error signal ($e_i = i^*_g - i_g$) is processed through the PR controller to generate the modulation signal ($m(t)$), normalized to the range [-1, 1], which is subsequently compared with the selected BCM carrier waveform to produce switching signals for the H6-IMPR inverter.

4) *BCM Waveform Selection Criteria:* The selection of the eight base carrier mark (BCM) configurations investigated in this study follows a systematic approach based on carrier frequency multiplication, waveform geometry, and their expected impact on common-mode voltage behavior. As illustrated in Fig. 3, the BCM configurations span a wide design space to comprehensively evaluate the relationship between carrier structure and system performance metrics, particularly leakage current suppression.

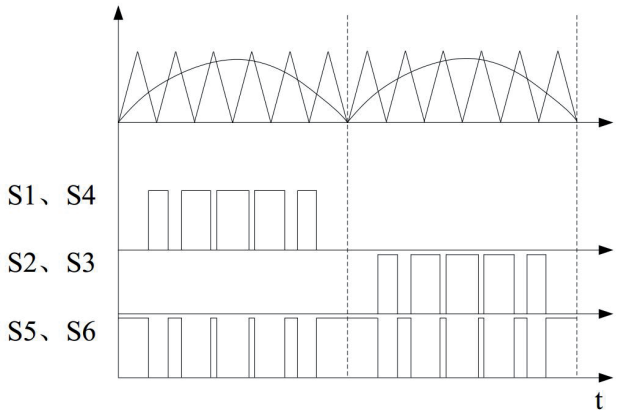

Fig. 2. Basic PWM structure (switching signals)

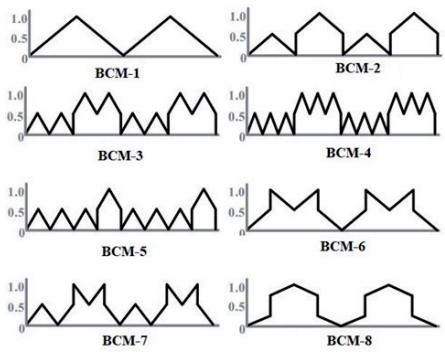

Fig. 3. Principal Base Carrier Mark (BCM) waveforms.

Rajiya Begum Sayyad, Upendar Jalla, A Novel Multi-Loop Base Carrier Mark PWM Strategy for Leakage Current Reduction in Grid-Connected Transformerless Inverters, Journal of Energy, vol. 74 Number 3 (2025), 3–11
https://doi.org/10.37798/2025743722

a) Carrier Waveform Geometry:

The fundamental distinction among BCM configurations lies in their geometric shape, which directly influences switching transition characteristics:

- **Triangular carriers (BCM-1, BCM-6):** Provide linear voltage transitions with constant dV/dt during rising and falling edges. BCM-1 employs two largetriangular waves per fundamental period ($2f_{sw}$), representing the conventional carrier approach. BCM6 uses four medium-sized triangular waves ($4f_{sw}$), offering a balance between switching frequency and harmonic distribution.
- **Trapezoidal carriers (BCM-2, BCM-8):** Incorporate flat-top regions that create extended dwell times at peak carrier values. These plateau regions maintain constant switching states, potentially reducing the number of transitions and associated dV_{cm}/dt spikes. BCM-2 combines trapezoidal and triangular elements, while BCM-8 employs pure trapezoidal waveforms.
- **Multi-triangular carriers (BCM-3, BCM-4, BCM-5, BCM-7):** Feature multiple high-frequency carrier cycles per fundamental period ($6-8f_{sw}$), creating more frequent but smaller-amplitude switching transitions. This category represents the core innovation of the proposed multi-loop approach, where increased carrier frequency enables finer control of common-mode voltage evolution.

b) Carrier Frequency Multiplication:

The effective switching frequency varies significantly across BCM configurations, creating distinct harmonic signatures and switching loss characteristics:

- **Base frequency ($2f_{sw}$):** BCM-1, BCM-2, and BCM8 operate at twice the fundamental switching frequency, providing conventional PWM performance with minimal switching losses but concentrated harmonic content around $2f_{sw}$ and its multiples.
- **Medium frequency ($4f_{sw}$):** BCM-6 doubles the carrier frequency relative to base configurations, offering improved harmonic spreading while maintaining moderate switching losses.
- **High frequency ($6-8f_{sw}$):** BCM-3, BCM-4, BCM5, and BCM-7 employ significantly elevated carrier frequencies, distributing harmonic energy across a broader spectrum. This frequency multiplication enables more uniform common-mode voltage transitions throughout the fundamental period.

c) Loop Rotation Classification:

The multi-loop designation refers to the pattern complexity and phase relationships embedded within carrier structures:

- **Sequential (conventional):** BCM-1, BCM-2, and BCM-8 follow traditional carrier patterns without complex phase rotations.
- **Single-loop rotation:** BCM-3 and BCM-4 implement consistent high-frequency triangular patterns with uniform phase relationships throughout the fundamental period. The small variations between BCM3 and BCM-4 arise from subtle phase adjustments intended to optimize switching instant distribution.
- **Two-loop rotation:** BCM-5 and BCM-6 introduce dual-pattern sequences where carrier characteristics alternate or vary systematically. BCM-5 exhibits non-uniform peak amplitudes, creating asymmetric switching patterns, while BCM-6 maintains uniform amplitudes but at medium frequency.
- **Three-loop rotation:** BCM-7 implements the most complex pattern with three distinct amplitude levels and phase relationships, designed to achieve sophisticated harmonic distribution and common-mode voltage shaping.

d) Common-Mode Voltage and Leakage Current Relationship:

The critical motivation for exploring diverse BCM structures stems from their direct impact on common-mode voltage (V_{cm}) and consequently leakage current. The instantaneous common-mode voltage in the H6-IMPR topology is given by:

$$V_{cm}(t) = \frac{V_{an}(t) + V_{bn}(t)}{2} \tag{4}$$

where V_{an} and V_{bn} are the voltages at inverter output points 'a' and 'b' relative to the neutral point. Different BCM configurations produce distinct switching state sequences, causing variations in $V_{cm}(t)$ evolution. The leakage current through parasitic capacitances (C_{pv}) between PV panels and ground is governed by:

$$i_{cm}(t) = C_{pv}\frac{dV_{cm}(t)}{dt} \tag{5}$$

Therefore, minimizing leakage current requires either: (a) maintaining constant V_{cm} (ideal but often impractical), or (b) minimizing dV_{cm}/dt by controlling switching transition rates and distributions.

Trapezoidal carriers (BCM-2, BCM-8) address this through extended dwell times with zero dV_{cm}/dt during plateau regions. High-frequency multi-triangular carriers (BCM-3 through BCM-7) take an alternative approach by distributing transitions more uniformly in time, potentially reducing peak dV_{cm}/dt values even if the average transition rate increases. The two-loop BCM-5 configuration combines both strategies with varied amplitude peaks and increased frequency, which, as demonstrated in the results, achieves superior leakage current suppression.

e) Design Space Exploration Strategy:

The systematic selection of these eight BCM configurations enables comprehensive evaluation of the multidimensional trade-offs inherent in carrier-based PWM design:

- BCM-1 serves as the baseline conventional triangular carrier reference
- BCM-2 and BCM-8 evaluate the impact of trapezoidal geometry
- BCM-3 and BCM-4 explore single-loop highfrequency approaches
- BCM-5 and BCM-6 investigate two-loop strategies with different frequency-amplitude combinations
- BCM-7 examines the most complex three-loop pattern

This comprehensive exploration strategy ensures identification of optimal configurations for specific performance priorities (leakage current, THD, efficiency, or V_{cm} stability) while revealing fundamental relationships between carrier structure and system behavior. Table II summarizes the key characteristics and design objectives of each BCM configuration.

Rajiya Begum Sayyad, Upendar Jalla, A Novel Multi-Loop Base Carrier Mark PWM Strategy for Leakage Current Reduction in Grid-Connected Transformerless Inverters, Journal of Energy, vol. 74 Number 3 (2025), 3–11
https://doi.org/10.37798/2025743722

TABLE II
CHARACTERISTICSANDDESIGNRATIONALEOFBCMCONFIGURATIONS.

BCM Type	Carrier Structure	Switching Frequency	Pattern Description	Primary Design Objective
BCM-1	Triangular wave	$2\times f_{sw}$	Two symmetric triangular carriers	Baseline conventional triangular carrier PWM
BCM-2	Trapezoidal -triangular	$2\times f_{sw}$	Mixed trapezoidal and triangular	Reduced switching stress with flat-top regions
BCM-3	Multi-triangular (single-loop)	$8\times f_{sw}$	High-frequency small triangular waves	Enhanced harmonic spreading (single-loop)
BCM-4	Multi-triangular (modified)	$8\times f_{sw}$	High-frequency with phase variations	Optimized single-loop with adjusted peaks
BCM-5	Multi-triangular (two-loop)	$6–8\times f_{sw}$	Medium-frequency with varied amplitudes	Balanced V_{cm} control (two-loop rotation)
BCM-6	Triangular (two-loop)	$4\times f_{sw}$	Medium-frequency larger triangular waves	Simplified two-loop with lower switching
BCM-7	Mixed amplitude (three-loop)	$6–8\times f_{sw}$	Non-uniform amplitude triangular pattern	Complex harmonic distribution (three-loop)
BCM-8	Trapezoidal wave	$2\times f_{sw}$	Two symmetric trapezoidal carriers	Minimum switching with extended dwell time

5) PWM Signal Generation Process: The PWM generation process integrates the modulation signal from the current controller with the selected BCM carrier structure: 1) The modulation signal $m(t)$ from the PR controller serves as the reference signal, normalized to the range [1, 1] and synchronized with the grid voltage through the PLL.

2) The selected BCM carrier waveform (BCM-1 through BCM-8) is generated using a dedicated carrier synthesis block that implements the specific geometric pattern and frequency multiplication ratio.

3) Comparator logic generates the primary switching signals by comparing the modulation signal against the BCM carrier. For the H6-IMPR topology with six switches, the switching logic is designed as:

$$S_1, S_4 = \begin{cases} 1, & \text{if } m(t) > 0 \text{ and } m(t) > BCM(t) \\ 0, & \text{otherwise} \end{cases} \tag{6}$$

$$S_2, S_3 = \begin{cases} 1, & \text{if } m(t) < 0 \text{ and } |m(t)| > BCM(t) \\ 0, & \text{otherwise} \end{cases} \tag{7}$$

$$S_5, S_6 = \begin{cases} S_6 = 1, S_5 = 0, & m(t) > 0, m(t) \le BCM(t) \\ S_5 = 1, S_6 = 0, & m(t) < 0, |m(t)| \le BCM(t) \\ 0, & \text{otherwise} \end{cases} \tag{8}$$

(8) This switching logic ensures the proper operating modes detailed in Table I, with switches S5 and S6 providing the freewheeling paths during zero voltage states.

4) Dead-time compensation is implemented to prevent shoot-through conditions during switching transitions. A fixed dead-time of t_{dead} = 2 μs is applied between complementary switch pairs (S1-S2 and S3-S4), with appropriate blanking logic to ensure that both switches in a leg are never simultaneously on.

5) Gate drive signal conditioning includes appropriate voltage levels (0-15V for the SiC MOSFETs specified in Table IV) and current drive capability to ensure fast switching transitions while minimizing switching losses and electromagnetic interference.

6) *Active and Reactive Power Control:* The active and reactive power delivered to the grid can be expressed in the stationary α-β reference frame as:

$$P = \frac{1}{2}(v_{g\alpha} i_{g\alpha} + v_{g\beta} i_{g\beta}) \tag{9}$$

$$Q = \frac{1}{2}(v_{g\beta} i_{g\alpha} - v_{g\alpha} i_{g\beta}) \tag{10}$$

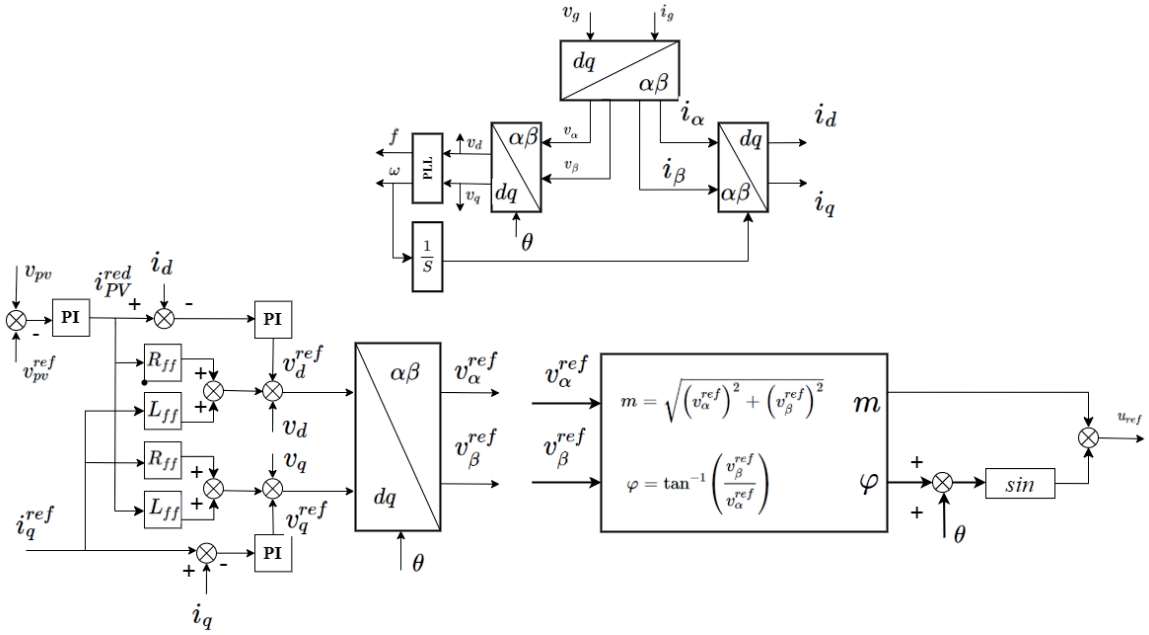

Fig. 4: Block diagram of control strategy for the PWM generation

Rajiya Begum Sayyad, Upendar Jalla, A Novel Multi-Loop Base Carrier Mark PWM Strategy for Leakage Current Reduction in Grid-Connected Transformerless Inverters, Journal of Energy, vol. 74 Number 3 (2025), 3–11
https://doi.org/10.37798/2025743722

For unity power factor operation, the current components in the α-β frame are controlled as:

$$i_{g\alpha} = I_g \cos(\phi) = I_g \tag{11}$$

$$i_{g\beta} = -I_g \sin(\phi) = 0 \tag{12}$$

where $\phi = 0$ represents the phase angle between voltage and current. This control strategy ensures that all delivered power is active power (P) with zero reactive power ($Q = 0$), maximizing system efficiency and minimizing grid current magnitude for a given power transfer. The unity power factor operation also ensures compliance with grid codes and minimizes unnecessary reactive current circulation that would increase losses in both the inverter and grid-side components.

The grid-injected current and voltage waveforms can be expressed in time domain as:

$$v_g(t) = V_g \cos(\omega_g t) \tag{13}$$

$$i_g(t) = I_g \cos(\omega_g t - \phi) = I_g \cos(\omega_g t) \tag{14}$$

where $V_g = 311.13$ V is the peak grid voltage amplitude and $\omega_g = 2\pi f_g = 314.16$ rad/s is the angular frequency corresponding to the 50 Hz grid frequency.

The control block diagram shown in Fig. 4 illustrates the comprehensive control strategy for PWM generation in the grid-connected system.

C. Leakage Current Management

A critical consideration in transformerless inverter design is the management of leakage current, which emerges due to the absence of galvanic isolation between the PV panel and grid system. Fig. 5 illustrates the residual current flow in the PV inverter without transformer.

The parasitic capacitances (C_{PV}) between PV cells/panel and ground lead to charge-discharge cycles with voltage fluctuations, resulting in residual current (i_{cm}) containing both low-frequency and switching high-frequency components. To ensure safe and efficient operation, the leakage current must adhere to standardized limits as specified in Table III.

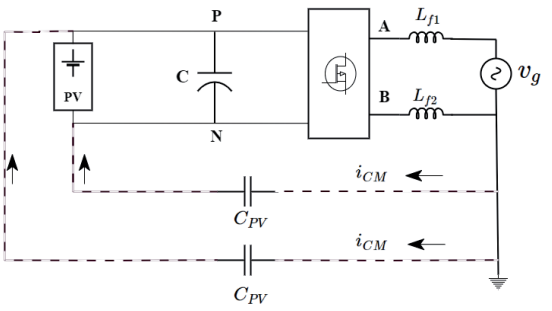

Fig. 5. Residual current flow in PV inverter without transformer.

Table III
Residual Current Limit Values (VDE 0126-1-1)

Fault Discontinuity Time (ms)	Leakage Current (mA)
300	30
150	60
40	150

These regulatory limits vary based on fault discontinuity time, with maximum allowable currents ranging from 30 mA to 150 mA depending on the duration of the fault condition. This regulatory compliance is essential for maintaining system safety and electromagnetic compatibility while minimizing power losses.

IV. Simulation Study

The simulation study was implemented using **Matlab/Simulink R2021b** environment with a fixed-step solver and a time step of 1×10^{-7} seconds to ensure accurate representation of high-frequency switching dynamics. The control algorithms were implemented using standard Simulink blocks.

Fig. 6 presents the comprehensive block diagram of the simulated system, illustrating the interconnection between the PV source, H6-IMPR inverter topology, LCL filter network, grid connection, and control subsystems. The control structure encompasses both inner current control loops and outer voltage regulation, with the PLL providing grid synchronization. The BCM generator block produces various carrier waveforms (BCM-1 through BCM-8) which are compared with the sinusoidal reference to generate appropriate gate signals for switches S1-S6.

The simulation investigation was conducted to evaluate the performance characteristics of a grid-connected transformerless H6-IMPR inverter system. The fundamental configuration, illustrated in Fig. 6, comprises an inverter coupled to the mains through a filtering network. The key parameters monitored during the simulation include the grid-injected current (I_g), the post-filter mains connection point voltage (V_g), and the inverter input bus voltage (V_{pv}). The system generates appropriate switching signals for the inverter's switches (S_1-S_6) based on various Base Carrier Mark (BCM) configurations.

The simulation environment was implemented using Matlab/Simulink, with the system parameters detailed in Table IV.

Table IV
System simulation parameters.

Parameter	Value
DC bus voltage V_{da}	400V
Output voltage V_g	311. 13 V
Grid frequency f_g Nominal	50 Hz
Power	14kW
Switching Frequency f_{sw}	10kHz
Filter Inductance (L_{f2},L_{f1})	6mH
Filter Capacitor C_f	2.0nF
Parasitic Capacitor C_{pv}	18nF
Switches (SCT3080ALGC11)	V_{dss} = 650V,$R_{ds(ON)}$ = 80mΩ,V_{sd} = 3.2V
Diodes (APT15D60B)	V_r = 600V,V_F = 1.9V

To comprehensively evaluate the system's performance, eight distinct states were examined, each corresponding to a different Base Carrier Mark configuration (BCM-1 through BCM-8), as outlined in Table V.

Table V
States simulation study.

State	Base Carrier Mark (BCM)
I	BCM-1
II	BCM-2
III	BCM-3
IV	BCM-4
V	BCM-5
VI	BCM-6
VII	BCM-7
VIII	BCM-8

Rajiya Begum Sayyad, Upendar Jalla, A Novel Multi-Loop Base Carrier Mark PWM Strategy for Leakage Current Reduction in Grid-Connected Transformerless Inverters, Journal of Energy, vol. 74 Number 3 (2025), 3–11
https://doi.org/10.37798/2025743722

The analysis focused on several key performance metrics: inverter efficiency (η), Total Harmonic Distortion (THD) of the output current, common mode voltage (V_{cm}), and leakage current (i_{cm}).

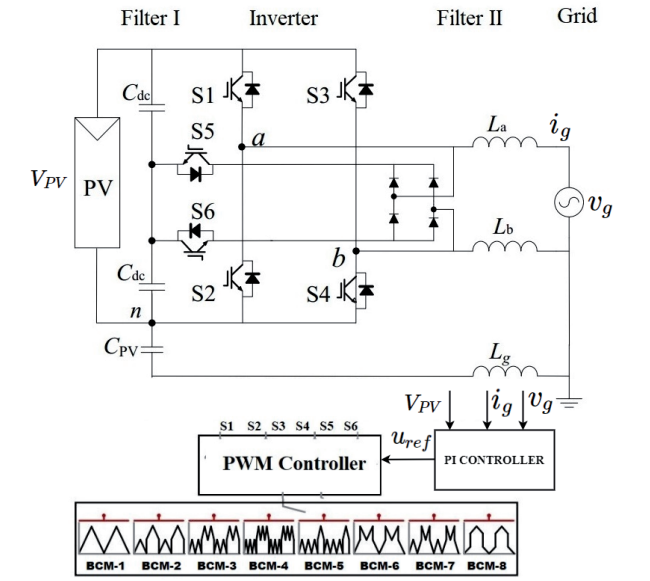

(a) Basic Block diagram

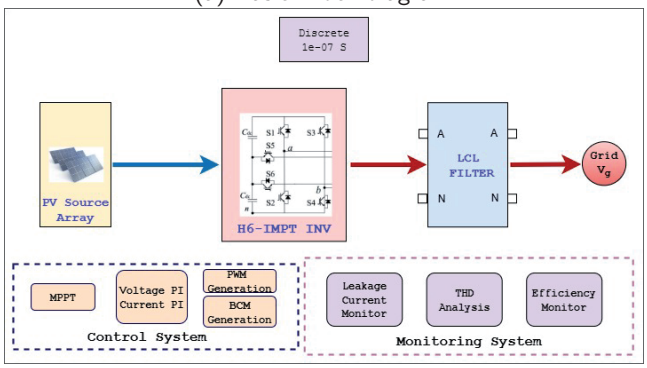

(b) MATLAB simulation block diagram

Fig. 6: Basic block diagram of the simulated system showing inverter connection to grid through filter

A. Total Harmonic Distortion Analysis

The analysis of Total Harmonic Distortion (THD) in the grid-injected current revealed significant variations across different BCM configurations, as illustrated in Fig. 7. The measured THD values ranged from 0.04% to 2.95%, demonstrating the substantial impact of carrier structure selection on output current quality.

STATE-II and STATE-IV PWM control schemes demonstrated the most favorable THD performance with exceptionally low values of 0.04%, representing nearideal sinusoidal current injection. STATE-I (0.09%) and STATE-VI (0.11%) also exhibited excellent performance. Conversely, STATE-V exhibited the highest THD at 2.95%, followed by STATE-VIII (2.07%) and STATEVII (2.02%). Despite these variations, all configurations remained well below the IEEE 519-2014 standard limit of 5% THD, ensuring full compliance with international power quality requirements.

An important observation is the inverse relationship between leakage current suppression and THD performance. STATE-V, which achieves the lowest leakage current (2.021 mA), exhibits the highest THD (2.95%). This trade-off suggests that asymmetric carrier patterns optimizing common-mode voltage behavior for leakage current reduction simultaneously introduce harmonic distortion. Conversely, STATE-II and STATE-IV achieve optimal THD but with moderate leakage current levels. The selection between these configurations depends on application priorities: BCM-2 or BCM-4 for maximum power quality, or BCM-5 for maximum leakage current suppression while maintaining regulatory compliance.

State	THD (grid current)
I	0.09%
II	0.04%
III	1.13%
IV	0.04%
V	2.95%
VI	0.11%
VII	2.02%
VIII	2.07%

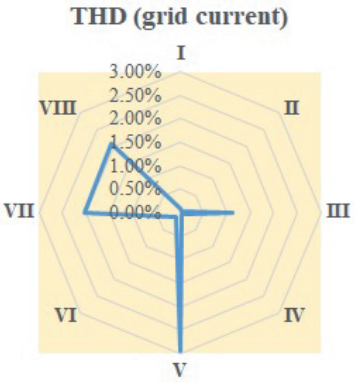

Fig. 7. THD grid current results for different type BCM

B. Common Mode Voltage Analysis

The common mode voltage (V_{cm}) analysis, presented in Fig. 8, revealed interesting patterns across different control configurations. Theoretically, the V_{cm} value should equate to $V_{pv}/2$. The experimental results demonstrated that STATE-III PWM control achieved the closest approximation to this ideal value compared to other configurations. This finding suggests that STATE-III PWM control offers superior common mode voltage characteristics, potentially contributing to enhanced system stability and reduced electromagnetic interference.

State	V_CM (AVERAGE)
I	201.315
II	201.312
III	201.134
IV	201.155
V	201.412
VI	201.221
VII	201.356
VIII	201.251

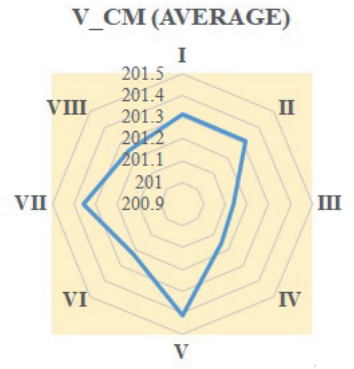

Fig. 8: Average common mode voltage V_{cm} results

C. Leakage Current Analysis

The investigation of leakage current (I_{cm}), depicted in Fig. 9, demonstrated that all PWM control configurations maintained leakage current levels below the standardspecified limit of 300mA. STATE-V PWM control exhibited the most favorable performance with the lowest leakage current values, while STATE-VIII PWM control resulted in the highest leakage current measurements. This variation in leakage current characteristics highlights the importance of control strategy selection in managing system safety and compliance requirements.

Rajiya Begum Sayyad, Upendar Jalla, A Novel Multi-Loop Base Carrier Mark PWM Strategy for Leakage Current Reduction in Grid-Connected Transformerless Inverters, Journal of Energy, vol. 74 Number 3 (2025), 3–11
https://doi.org/10.37798/2025743722

TABLE VI
MEASURED PEAK LEAKAGE CURRENT VALUES FOR ALL BCM CONFIGURATIONS.

State	BCM Type	Peak I_{cm} (mA)	Compliance Status
I	BCM-1	5.441	√Pass
II	BCM-2	4.2641	√Pass
III	BCM-3	3.5451	√Pass
IV	BCM-4	3.3541	√Pass
V	BCM-5	2.021	√Pass (Best)
VI	BCM-6	5.4491	√Pass
VII	BCM-7	4.5999	√Pass
VIII	BCM-8	7.7551	√Pass
VDE 0126-1-1 Limit (40ms discontinuity)			150 mA
Conservative Design Limit			300 mA

It should be noted that while Table III presents the regulatory limits specified in VDE 0126-1-1 standard, industrial practice often adopts more conservative design thresholds. Throughout this work, we reference a conservative design limit of 300 mA to ensure robust safety margins across varying environmental and operating conditions, while maintaining compliance with the stricter 150 mA regulatory limit for 40ms fault discontinuity time.

The investigation of leakage current (I_{cm}), depicted in Fig. 9 and quantified in Table VI, demonstrated that all PWM control configurations maintained leakage current levels significantly below both the VDE 0126-1-1 standard limit of 150 mA (for 40ms fault discontinuity time) and the conservative design threshold of 300 mA. The measured peak leakage current values ranged from 2.021 mA (STATE-V) to 7.7551 mA (STATE-VIII), representing merely 1.35% to 5.17% of the regulatory limit.

STATE-V PWM control exhibited the most favorable performance with 2.021 mA, demonstrating a 73.9% reduction compared to STATE-VIII. Other notable lowleakage configurations include STATE-IV (3.3541 mA) and STATE-III (3.5451 mA). Even the worst-performing configuration maintains leakage current at only 2.59% of the conservative design threshold, demonstrating the effectiveness of all proposed multi-loop BCM strategies. The superior performance of STATE-V is attributed to its two-loop carrier rotation pattern, which effectively minimizes common-mode voltage variations and reduces high-frequency components in the parasitic capacitance charging/discharging cycles.

D. Efficiency Analysis

The efficiency analysis, illustrated in Fig. 10, revealed a clear correlation between BCM configuration and system performance. Under the tested operating conditions, STATE-VIII PWM control, utilizing the BCM VIII waveform, demonstrated the lowest efficiency levels. Conversely, STATE-IV PWM control, implementing the BCM-IV waveform, achieved the highest efficiency ratings. This significant variation in efficiency metrics emphasizes the critical role of BCM waveform selection in optimizing system performance.

State	I_CM (RMS)
I	5.441
II	4.2641
III	3.5451
IV	3.3541
V	2.021
VI	5.4491
VII	4.5999
VIII	7.7551

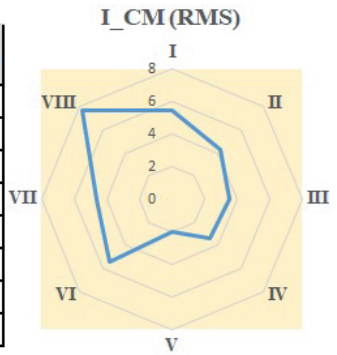

Fig. 9 Leakage Current values for different type BCM control

State	η (efficiency)
I	98.103
II	98.101
III	98.1
IV	98.141
V	98.079
VI	98.103
VII	98.051
VIII	97.781

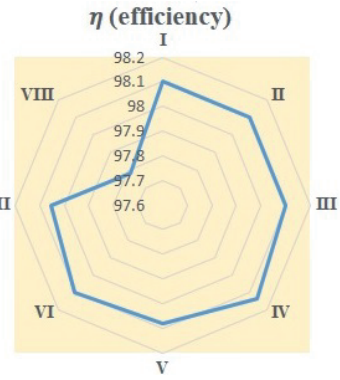

Fig. 10. Efficiency values for different BCM control

The comprehensive analysis of these performance metrics provides valuable insights into the optimization of grid-connected transformerless inverter systems. The results demonstrate that different BCM configurations offer distinct advantages and trade-offs across various performance parameters, necessitating careful consideration in system design and implementation.

V. CONCLUSION

This research introduces and validates a novel multiloop BCM-based PWM strategy for leakage current reduction in transformerless inverters. The comprehensive evaluation of eight distinct BCM configurations reveals the superior performance of the proposed approach, particularly in addressing the critical challenge of leakage current suppression. The STATE-V configuration of the multi-loop BCM strategy demonstrates exceptional capability in minimizing leakage current while maintaining compliance with safety standards, representing a significant advancement in transformerless inverter technology. The study's findings highlight the effectiveness of combining different carrier rotation techniques in BCM generation, resulting in optimized system performance across multiple metrics. While STATE-V excels in leakage current suppression, other configurations show strengths in specific areas: STATEII & IV achieves superior THD performance, STATEIII optimizes common mode voltage characteristics, and STATE-IV maximizes system efficiency. This comprehensive performance evaluation provides valuable insights for system designers, enabling informed decisions based on specific application requirements. The proposed multi-loop BCM strategy represents a practical and effective solution to one of the most significant challenges in transformerless PV inverter design. Future research could focus on developing adaptive switching strategies between different BCM configurations based on real-time grid conditions and exploring the integration of artificial intelligence techniques for optimal BCM selection. These advancements would further enhance the applicability of transformerless inverters in next-generation renewable energy systems.

Rajiya Begum Sayyad, Upendar Jalla, A Novel Multi-Loop Base Carrier Mark PWM Strategy for Leakage Current Reduction in Grid-Connected Transformerless Inverters, Journal of Energy, vol. 74 Number 3 (2025), 3–11
https://doi.org/10.37798/2025743722

References

[1] P. Bocquillon, *Climate and Energy Transitions in Times of Environmental Backlash? The European Union 'Green Deal' From Adoption to Implementation*, Journal of Common Market Studies, 2024. DOI: 10.1111/jcms.13675.

[2] Zhu Ce, Shengyuan Xiao, and Yun Yang, *Leakage current suppression methods for single-phase photovoltaic inverters*, Applied and Computational Engineering, vol. 78, no. 1, pp. 3140, 2024.

[3] C. A. De Carvalho Caique, P. R. D. R. Da Silva Paulo, J. A. Pomílio José Antenor, and J. M. Araújo José Mário, *Leakage Current Mitigation in Transformerless Grid-Connected PV Inverters Through Level Modulation Switching*, 2023. DOI: 10.1109/spec56436.2023.10407919.

[4] M Mohan et al., *Switched Inductor Based Transformerless Boost Inverter*, Materials Today: Proceedings, vol. 58, no. 1, pp. 496503, 2022.

[5] B. Çavdar et al., *Frequency Stability Analysis of Active Power Control Methods in Large-Scale Photovoltaic Power Plants*, EMO Scientific Journal, vol. 11, no. 21, pp. 17-27, 2021.

[6] S. He et al., *Modeling and Suppression of Zero-Sequence Circulating Current Resonance for Parallel Interleaved Inverters with Bypass Capacitor-Based Leakage Current Mitigation*, IEEE Journal of Emerging and Selected Topics in Power Electronics, vol. 11, no. 3 (June), year: 2023.

[7] S. Li et al., *A Modified Carrier-Based Discontinuous PWM for Photovoltaic Three-Level Converter with Reduced Common Mode Voltage Ripple*, In Proceedings of the International Conference on Power and Energy Technology (ICPET), year: 2023 DOI:10.1109/ICPET59380.2023.10367527.

[8] Yikun Wang, *Innovative approaches for minimizing leakage current in three-phase transformerless PV inverters*, Journal of Physics, vol. 2795, no. 1, pp. 012017, 2024. DOI: 10.1088/17426596/2795/1.

[9] C.C.A de Carvalho et al., *Leakage Current Mitigation in Transformerless Grid-Connected PV Inverters Through Level Modulation Switching*, In Proceedings of the IEEE Power Electronics Specialists Conference (SPEC), pp. 10407919-1, 2023.

[10] Tingrui Mao et al., *Transformerless Grid-connected PV Converter With Leakage Current Suppression Ability: A Novel Solution Based on Active Zero-Sequence Current Injections*, In Proceedings of the IEEE Energy Conversion Congress and Exposition-Asia (IPCM-ECCE Asia), pp. 10567375-1, 2024.

[11] Tingrui Mao, Xiuyun Wang, Chuang Liu, Dongbo Guo, Rutian Wang, Ruifeng Li, Qinhai Yu, and Zhongchen Pei, *Transformerless Grid-connected PV Converter With Leakage Current Suppression Ability: A novel solution based on active zero-sequence current injections*, 2024. DOI: 10.1109/ipemcecceasia60879.2024.10567375.

[12] Christopher J. Rodríguez-Cortés, José M. Sosa, P. R. Martinez, Gerardo Vázquez-Guzmán, and Adolfo Núñez, *Overview on Leakage Current Reduction Methods in Single-Phase Grid-Connected Inverters*, 2023. DOI: 10.1109/ropec58757.2023.10409442.

[13] Geye Lu, Jianzhen Qu, Dayong Zheng, and Pinjia Zhang, *An Improved Leakage-current-based Online Monitoring Method of Transformer Insulation by Injecting Asymmetric Voltages at Photovoltaic Inverter Switching Frequency*, pp. 4826-4831, 2023. DOI: 10.1109/icems59686.2023.10345064.

[14] Xiaolong Xiao, Rui Sun, Yaqian Li, and Huafeng Xiao, *Collecting Leakage Current and Suppression Strategy for Non-Isolated Photovoltaic Grid-Connected System*, pp. 158-162, 2023. DOI: 10.1109/peas58692.2023.10394811.

[15] X. Xiao et al., *Collecting Leakage Current and Suppression Strategy for Non-Isolated Photovoltaic Grid-Connected System*, In Proceedings of the IEEE Power Electronics and Applications Symposium (PEAS), pp. 10394811-158, 2023.

[16] Qiang Lou, Jang J.M., and Cheng K.W.E., *A Novel SinglePhase Five-Level Transformerless Inverter Topology with Common-Mode Voltage Suppression for PV Applications*, IEEE Transactions on Power Electronics, vol. 39, no. 3, pp. 2893-2907, 2024.

[17] C. J. Rodríguez-Cortés et al., *Overview on Leakage Current Reduction Methods in Single-Phase Grid-Connected Inverters*, In Proceedings of the IEEE Region Ochomurense Power Electronics Symposium (ROPEC), pp. 10409442-1, 2023.

[18] G. Lu et al., *An Improved Leakage-current-based Online Monitoring Method of Transformer Insulation by Injecting Asymmetric Voltages at Photovoltaic Inverter Switching Frequency*, In Proceedings of the International Conference on Electrical Machines and Systems (ICEMS), pp. 10345064-4826, 2023.

[19] S. R. Begum and J Upendar,*Development of Improved Lowleakage Current H6 Single-Phase Full-Bridge Inverter Topology*, Indian Journal of Science and Technology , vol .17 , no .17 , pp .1813–1823 , year :2024 , DOI :10 .17485 /IJST/v17i17 .280 .

Journal of Energy

VOLUME 74 Number 3 | 2025

journal homepage: http://journalofenergy.com/

An Economy Aspect of Different Nuclear Energy Development

Dinka Lale, Dubravko Pevec, Mario Matijević

Summary — Humanity must face the reality that it cannot depend indefinitely on combustion of coal, gas and oil for most of its energy needs. In the long term, nuclear energy seems to be the only one capable of replacing fossil fuel energy in the production of electricity in the world. The specific greenhouses gases (GHG) emissions of nuclear power plants are among the lowest of any electricity generation method. Nuclear power is cost-competitive with other forms of electricity generation, except where there is direct access to low-cost fossil fuels.

Global primary energy needs rise more slowly than in the past, but still an increase of 19% between today and 2050 is expected according to World Energy Outlook 2022. Electrical energy needs will rise faster than primary energy needs and the electrical energy production has to be with low GHG emissions due to global warming mitigation. We assume in our scenarios that nuclear energy will be global electricity production leader with a percentage of 36.7 % in the year 2050. In addition, we assume that all thermal power plants will be replaced by uranium or thorium fuel cycle nuclear power plants by the year 2057.

This paper describes a comparison of different long term nuclear energy development scenarios according to costs. The calculated saving of GHG emissions in case of significant use of nuclear energy in the future in the world is emphasized.

Keywords — **Climate change, Economy aspect, Nuclear energy, GHG emissions**

I. Introduction

Global warming is a big problem that humanity is facing, so we have to find a solution soon. Energy needs are increased by the economic development and the constant increase in earth population. On the other side, the production and use of primary and electrical energy cause the release of carbon dioxide into the atmosphere. Green House Gas (GHG) emissions are the main cause for climate change, which is increasingly affecting planet Earth [1] [2]. Global GHG emissions increased by 1.2 per cent from 2021 to 2022 to reach a new record of 57.4 gigatons of CO_2 equivalent ($GtCO_2e$) [3]. Global energy-related CO_2 emissions grew by 0.9% or 321 Mt in 2022, reaching a new high of over 36.8 Gt [4]. Humanity is in constant search for new energy sources to meet its own energy needs.

Corresponding author: Dinka Lale

Dinka Lale is with University of Dubrovnik Faculty of electrical engineering and applied computing, Dubrovnik, Croatia (email: dinka.lale@unidu.hr)

Dubravko Pevec and Mario Matijević are with the University of Zagreb Faculty of Electrical Engineering and Computing, Zagreb, Croatia (emails: dubravko.pevec@fer.hr; mario.matijevic@fer.hr).

The global population growth projection are from 7.8 billion people in 2021 to 8.5 billion in 2030 and 9.7 billion in 2050. The energy, mineral, and carbon prices projections are given by the IEA (International Energy Agency) and presented in 3 different scenarios. NZE (Net Zero Emissions by 2050 Scenario) sets out a pathway to the stabilisation of global average temperatures at 1.5 °C above pre–industrial levels. Announced Pledges Scenario (APS) assumes that governments will meet, in full and on time, all of the climate–related commitments that they have announced, including longer term net zero emissions targets. Stated Policies Scenario (STEPS) looks not at what governments say they will achieve, but at what they are actually doing to reach the targets and objectives that they have set out [2].

Global electricity demand climbed to 24700 TWh in 2021 – an increase of 6% from the previous year and the biggest annual increase since 2010 – reflecting a rebound in many economies following the pandemic. The largest electricity consumers are China, United States and Europe. Together, they account for over 60% of global electricity demand [2].

Renewable energy technologies currently provide close to 30% of electricity generation and are set for rapid growth in all scenarios, led by solar photovoltaics (PV) and wind. In the NZE Scenario (WEO 2022) the share of renewables in electricity generation rises from 28% in 2021 to over 60% in 2030, and nearly 90% in 2050 (shown in Figure 1) [2].

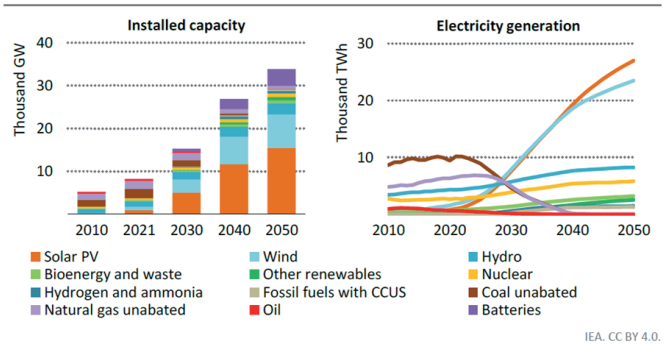

Fig. 1. "Total installed capacity and electricity generation by source in the NZE Scenario, 2010-2050"

In general, the predictions in WEO 2022 related to renewable energy sources are that renewables, notably solar PV and wind, gain the most ground of any energy source this decade, accounting for 43% of electricity generation worldwide in 2030, up from 28% today.

Dinka Lale, Dubravko Pevec, Mario Matijević, An Economy Aspect of Different Nuclear Energy Development, Journal of Energy, vol. 74 Number 3 (2025), 12–16
https://doi.org/10.37798/2025743722

It is important to take into account both finances and environmental impact when planning investments in the electric power system. Nuclear energy has proven to be one of the most profitable [5] [6] [7] [8]. Figure 2 [5] shows the effect of discount rate on levelized cost of electricity (LCOE) for different technologies (source: OECD Nuclear Energy Agency).

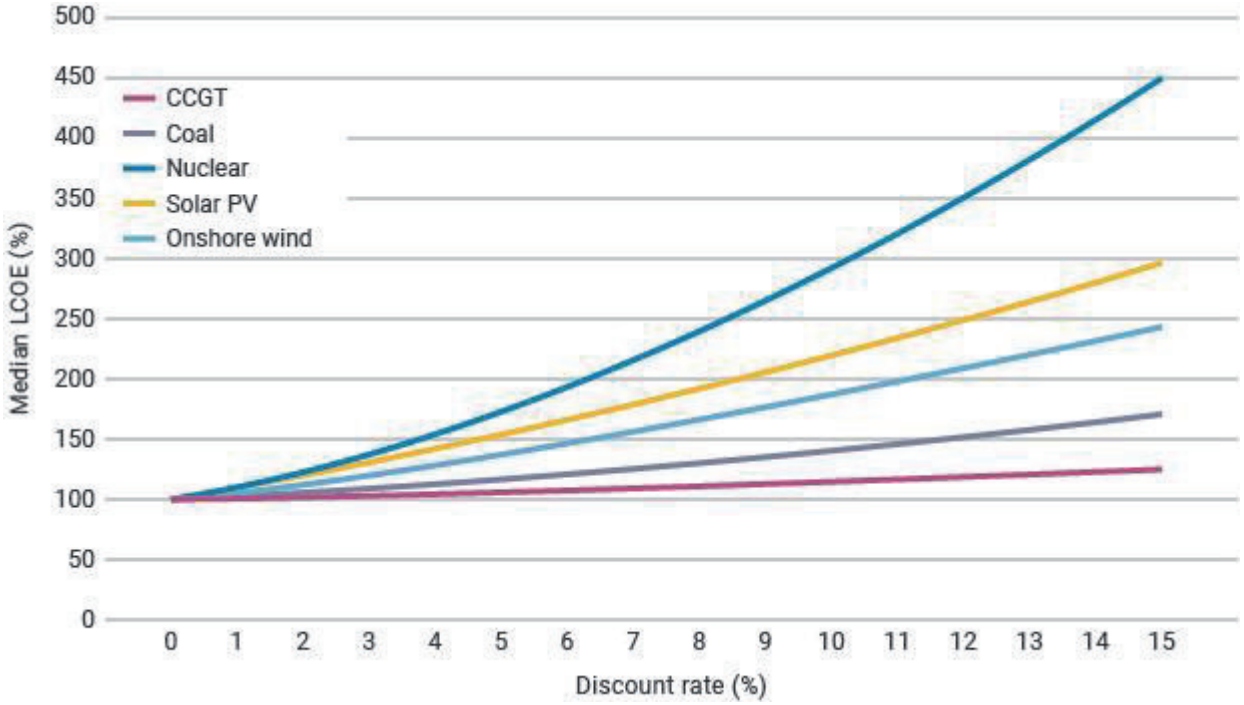

Fig. 2. Effect of discount rate on levelized costs of electricity (LCOE)

At a 3% discount rate, nuclear is the lowest cost option for all countries [5].

Nuclear energy averages 0.4 euro ¢/kWh, much the same as hydro, coal is over 4.0 ¢/kWh and gas ranges 1.3-2.3 ¢/kWh [6].

Fig. 3. Average life-cycle CO2 equivalent emissions

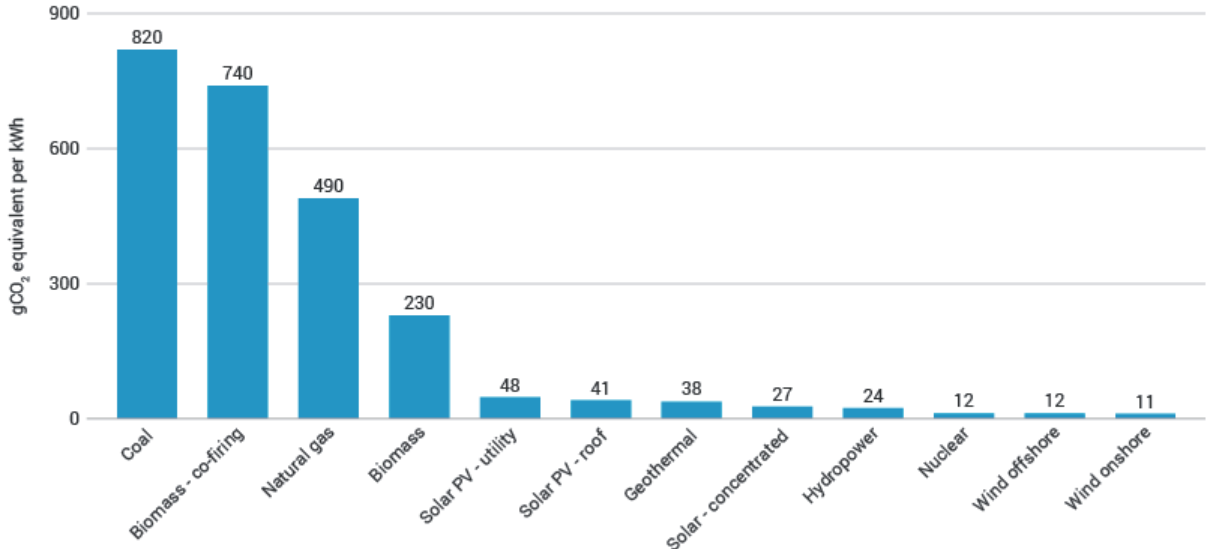

UN IPCC has provided a median value among peer-reviewed studies of 12 g CO_2 equivalent/kWh for nuclear, similar to wind and lower than all types of solar as described in Figure 3.

In March 2022 the United Nations Economic Commission for Europe (UNECE) estimated a range of 5.1 – 6.4 g CO_2 equivalent per kWh for nuclear, the lowest among all low-carbon technologies.

The transport and energy production are the largest emitters of GHG into the atmosphere. Electricity production in nuclear power plants causes very low GHG emissions. It is therefore necessary to increase the share of nuclear power plants in the future [2] [9]. A further question is which type of nuclear power plants to prefer considering the price and radioactive waste [10].

Pressurized Water Reactors (PWR) are the most developed and currently the most widely used. However, from the point of view of the produced radioactive waste, the use of Fast Breeder Reactor (FBR) and reactors that use thorium is more favourable. It cannot be expected that newer types of reactors will be used to a greater extent any time soon. But it is necessary to take into account their advantages and think about their use in the future [1].

Nuclear power plant construction is typical of large infrastructure projects around the world. Despite this, nuclear power plant costs and delivery challenges tend to be under-estimated [11].

II. Scenarios

We assume 3 different scenarios according to different share of nuclear energy in the total energy produced. Scenario 1 predicts

Dinka Lale, Dubravko Pevec, Mario Matijević, An Economy Aspect of Different Nuclear Energy Development, Journal of Energy, vol. 74 Number 3 (2025), 12–16
https://doi.org/10.37798/2025743722

an increase in the use of nuclear energy that follows the increase in the total world production of electricity, so that the share of nuclear energy will be around 9% by 2070. Scenario 2 assumes a high increase in nuclear capacity by 2100. This Scenario predicts that in 2040, nuclear energy will have a share of 25% in the total world electricity production. In 2070, it is predicted that all fossil fuel power plants will be phased out, and the share of nuclear energy will be 44%. Scenario 3 assume a very significant increase in nuclear capacity by the end of the century. Scenario 3 predicts that all fossil fuel power plants will be phased out in 2057, when the share of nuclear energy in the total world electricity production will be 51%.

In Scenario 1 we assumed very small increase in the use of nuclear energy in the future. Table 1 shows nuclear energy share, fossil fuel power energy's share and the share of renewable energy sources with hydropower plants (RES) for Scenario 1. At the same time, the use of fossil fuel power plants is slowly decreasing.

Table I
Nuclear Share, Fossil Fuel Power Plant Share and RES Share (%) in Total Energy Production by the End of a Century for Scenario I

The year	Nuclear energy share (%)	Fossil fuel power plant share (%)	The share of RES (including hydropower plants) (%)
2030	10.5	52.1	37.4
2040	9.4	42.5	48.1
2050	9.0	34.8	56.2
2060	9.4	28.4	62.2
2070	9.9	23.2	66.9
2080	10.4	19.0	70.6
2090	10.9	15.5	73.6
2100	11.5	12.7	75.8

It is very ungrateful and unrealistic to assume that the largest share of electricity produced in the future will come from renewable energy sources. This Scenario was intended to show that nuclear energy should be more represented in the overall production of electricity due to its economy. Apart from the fact that it is a constant and safe source of electricity, it is financially very favourable. The ecological aspect will be discussed later, too. It will also be shown that nuclear energy is favourable in terms of environmental impact and carbon dioxide emissions into the atmosphere. Nevertheless, it is assumed that an efficient way of energy storage will be found in the future.

In Scenario 2 we assumed moderate reduction in the use of fossil fuel power plants. Table 2 shows the share of nuclear capacity, thermal power plants and the share of renewable energy sources for Scenario 2 by the end of the century.

Table II
The Share of Nuclear Power Plants, Fossil Fuel Plants and Plants Based on RES (Including Hydropower Plants) (%) in the Production of Electricity in The World by the End of the Century for Scenario 2

The year	Nuclear energy share (%)	Thermal power plant share (%)	The share of RES (including hydropower plants) (%)
2030	11.8	52.0	36.2
2040	25.8	31.2	43.0
2050	34.7	10.9	54.4
2060	43.7	3.8	52.5
2070	44.5	0	55.5
2080	45.4	0	54.6
2090	46.3	0	53.7
2100	47.2	0	52.8

The increase in the share of nuclear energy is high. The share of use of fossil fuel power plants is continuously decreasing. Fossil fuel power plants are the biggest polluters of all electricity production facilities. For this reason, efforts are being made to reduce the use of fossil fuel power plants in the future due to limited fossil fuel supplies. At the same time, the development and utilization of technologies using renewable energy sources are encouraged. Poland, where the share of fossil fuels in electricity production was 73% in 2023, can be taken as an example. Thus, Poland is responsible for as much as 0.89% of the total global CO_2 emissions [12]. Annual CO_2 emission in Poland amounts to approximately 340 million tonnes (227 billion m^3). Compared to the emissions in the European Union, Poland was ranked as the fourth country with the largest greenhouse gas emissions (GHG) in 2018 which causes a major air pollution problem [13]. In 2010 Poland lost 48544 years of life to air pollution. Economic cost from air pollution was US$ 101 billion [14]. Despite significant efforts to reduce polluting air emissions, during and after the economic transition in the 1990s, Poland remains home to many of the most polluted cities in the European Union (EU). Annual average ambient concentrations of fine particulate matter (PM 2.5 concentrations) are often multiple times the maximum levels allowed under EU law (25 $\mu g/m^3$) and the WHO (World Health Organisation) air quality guideline value (10 $\mu g/m^3$). The most widespread exceeds of EU air quality Limit Values are seen in south and southwestern Poland [15].

In Scenario 3 we assume a very significant increase in nuclear capacity by the end of the century and the complete abolition of fossil fuel power plants by 2057. Table 3 shows the assumed increase.

Table III
The Share of Nuclear Power Plants, Fossil Fuel Plants and Plants Based on RES (Including Hydropower Plants) (%) in The Production of Electricity in the World by the End of the Century for Scenario 3

The year	Nuclear energy share (%)	Thermal power plant share (%)	The share of RES (including hydropower plants) (%)
2030	13.9	40.6	45.5
2040	22.7	17.6	59.7
2050	36.7	6.1	57.2
2060	58.7	0	41.3
2070	59.9	0	40.1
2080	61.1	0	38.9
2090	62.3	0	37.7
2100	63.5	0	36.5

Renewable energy sources and hydropower take the largest share for the first couple of decades while conditions are created for a large increase in the share of nuclear energy in Scenario 3.

The use of renewable energy sources has greatly increased in developed countries in the last few decades. The assumption is that this increase will be even greater in the coming years as we discussed already in the introduction. A large increase in the use of renewable energy sources (especially wind generators and solar photovoltaic technology) is still expected in developing countries.

III. Levelised Cost of Electricity

WEO 2022 uses the levelised cost of electricity (LCOE) as a well established, transparent, and intuitive metric, widely used in policy making, modelling and public discussion [5]. It is the total cost to build and operate a power plant over its lifetime divided by the total electricity output dispatched from the plant over that period, hence typically cost per megawatt hour. It takes into

Dinka Lale, Dubravko Pevec, Mario Matijević, An Economy Aspect of Different Nuclear Energy Development, Journal of Energy, vol. 74 Number 3 (2025), 12–16
https://doi.org/10.37798/2025743722

account the financing costs of the capital component (not just the 'overnight' cost) [11]. We will use the value LCOE but a little bit modified. We used the mean LCOE value that we obtained as the LCOE arithmetic mean of all systems larger than 1 MW.

We calculated average LCOE for nuclear power plants and fossil fuel power plants and they are 44.74 USD/MWh and 92.57 USD/MWh, respectively.

Predictions for the use of different renewable energy sources in the future from WEO2022 were taken into account. The average value for solar technology, onshore wind technology, offshore wind technology, hydropower technology and biomass is calculated. LCOE for solar technology, wind technology, hydropower, and biomass is 68.16 USD/MWh, 72.82 USD/MWh, 77.64 USD/MWh, and 88.56 USD/MWh, respectively. Then, the average LCOE value for renewable energy sources is calculated according to what proportion of which source will be used in the future. These predictions are taken from WEO 2022.

IV. Results

We used the data of the total produced electricity from Chapter 2 and the mean LCOE value from Chapter 3. After the calculation, the following figures are obtained.

The Figure 4 shows the distribution of financial resources invested in different types of power plants (fossil fuel power plants, nuclear power plants and renewable energy power plants) for Scenario 1 until the end of the century.

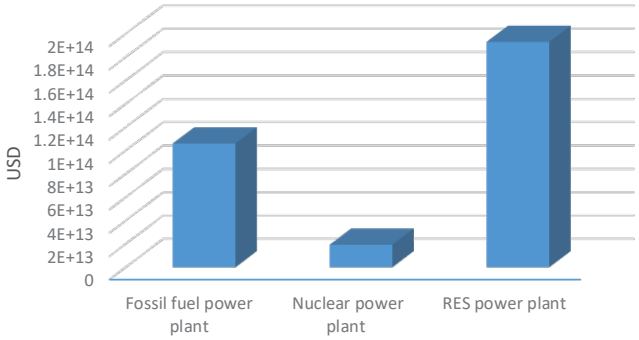

Fig. 4. Costs for the Scenario 1

The Figure 5 shows the distribution of financial resources invested in different types of power plants (fossil fuel power plants, nuclear power plants and renewable energy power plants) for Scenario 2 until the end of the century.

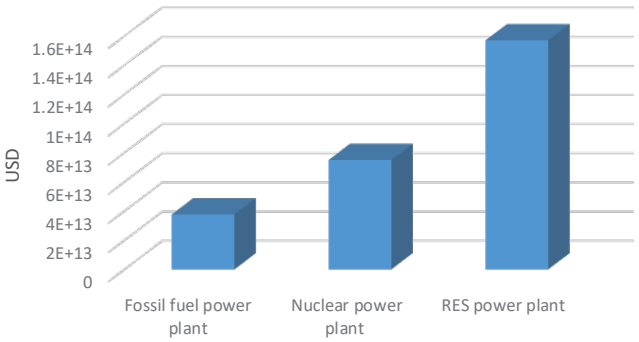

Fig. 5. Costs for the Scenario 2

The Figure 6 shows the distribution of financial resources invested in different types of power plants (fossil fuel power plants, nuclear power plants and renewable energy power plants) for Scenario 3 until the end of the century.

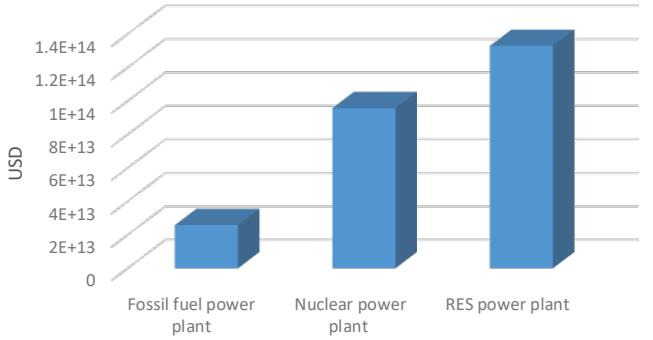

Fig. 6. Costs for the Scenario 3

The Figure 7 shows a comparison of the costs for all three scenarios to the year 2100.

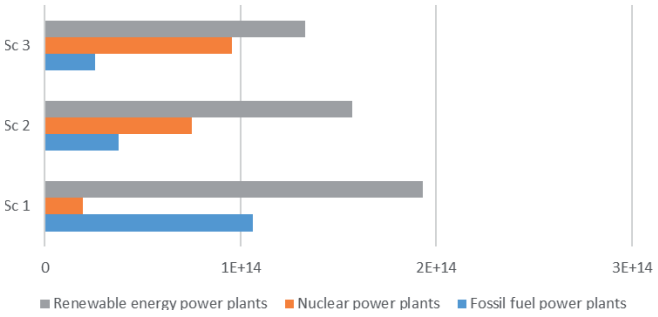

Fig. 7. The comparison of costs for all 3 scenarios by the end of the century

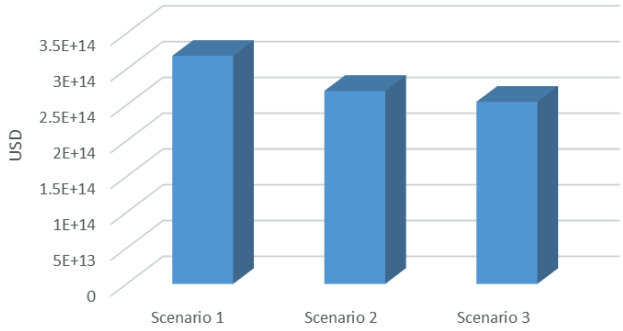

Fig. 8. The total costs for all 3 scenarios by the year 2100.

From the Figure 8 it is evident that the most money for produced electricity in the world by the end of the century is spent in the first Scenario. The first Scenario implies the smallest increase in the use of nuclear energy in the future. From the Figure 8 we can see that electrical energy in kWh obtained from nuclear sources results in the lowest financing costs for a long time.

It is preferable to use nuclear energy in combination with energy from renewable energy sources due to the low impact on the environment and climate change.

V. GHG Emissions

Another important factor affecting electricity markets is the cost of carbon dioxide (CO_2) emissions, which should make nuclear power more attractive by raising the costs of fossil-fired competitors [16]. Using data for GHG emissions per produced TWh of electricity from different energy sources [17], [18], mean values were calculated for each source of electrical energy individually. Predictions for the use of different types of fossil fuels and renewable energy sources in the future from WEO 2022 were also taken into account.

Dinka Lale, Dubravko Pevec, Mario Matijević, An Economy Aspect of Different Nuclear Energy Development, Journal of Energy, vol. 74 Number 3 (2025), 12–16
https://doi.org/10.37798/2025743722

The calculated values for GHG emissions are presented in Figure 9. Scenario 1 has by far the highest CO_2 emissions compared to Scenario 2 and Scenario 3. This is especially evident from the column (red) showing the assumed emissions from fossil power plants (Figure 9.).

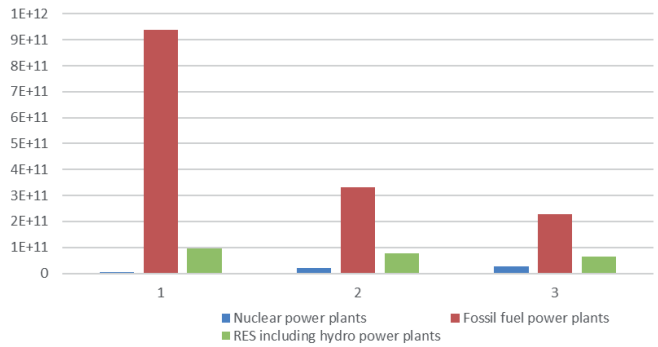

Figure 9. GHG emissions according to energy sources for Scenario 1, 2 and 3

VI. Conclusion

Electricity production is one of the strategic plans of every country. Most countries in the world have to plan electricity production with their neighbours as well as countries in the wider region. It is known that nuclear energy is a safe and reliable source of electricity. In addition, it is an energy source that is environmentally friendly due to low GHG emissions.

In this paper, scenarios were analysed that predict a medium, high and very high share of the use of nuclear energy in the world by the end of this century. It turned out, as we expected, that nuclear energy is among the most profitable energy sources. In scenarios predicting a higher percentage of nuclear power than today, less money was spent than in scenarios with a low nuclear power share.

Nuclear energy, in addition to being a safe, reliable, and environmentally friendly source, is also an economically very profitable source of electricity.

References

[1] D. Lale, "Estimation of nuclear fuel supply sufficiency in the case of significant nuclear energy contribution to the solution of the global warming problem", doctoral thesis, University of Zagreb, Faculty of electrical engineering and computing, 2020

[2] International Energy Agency, World Energy Outlook 2022, November 2022

[3] https://www.unep.org/interactives/emissions-gap-report/2023/#section-1 – UN environment programme "Emissions Gap Report 2023"

[4] https://www.iea.org/reports/co2-emissions-in-2022 – IEA Report "CO_2 Emissions in 2022", Growth in emissions lower than feared, 2023

[5] International Energy Agency and Nuclear Energy Agency, Projected Costs of Generating Electricity, 2020 Edition, Organisation for Economic Co-operation and Development/Nuclear Energy Agency, 46, quai Alphonse Le Gallo, 92100 Boulogne-Billancourt, France

[6] World Nuclear Association – Economics of Nuclear Power, update 29 September 2023

[7] D. Basu, V. W. Miroshnik, "The Political Economy of Nuclear Energy", Prospect and Retrospect, the book, Springer, 2019

[8] V. Knapp, D. Pevec, „Promises and limitations of nuclear fission energy in combating climate change", Energy Policy, Volume 120, 2018., str. 94-99

[9] D. Pevec, V. Knapp, M. Matijević, "Availability of the nuclear fuel for long-term expansion of nuclear power", *Proceedings of the 8th International Conference on Nuclear Option in Countries with Small and Medium Electricity Grids*, Dubrovnik, Croatia, 2010.

[1] D. Lale, D. Pevec, V. Knapp, M. Matijević, A Comparison of the Radioactive Waste Produced for Different Nuclear Energy Development Scenarios, *In Proceedings of the 13th International Conference of the Croatian Nuclear Society*, Zadar, Croatia, 5-8 June 2022, pp 118-1 (for a paper in the conference proceedings)

[1] World Nuclear Association, https://world-nuclear.org/Information-Library/Economic-Aspects/Economics-of-Nuclear-Power (accessed 13th of May 2024)

[1] web: https://www.worldometers.info/co2-emissions/poland-co2-emissions/ , accessed: May 2024

[10] Joanna Fabiszewska-Solares, Krzysztof Kobyłka, Kamil Laskowski, Karolina Marszał, Aleksander Śniegocki, "Assessment of current state, past experiences and potential for CCS deployment in the CEE region", The Building momentum for the long-term CCS deployment in the CEE region 2021

[11] Nikolay Vasev, Governing energy while neglecting health – The case of Poland, Health Policy, Volume 121, Issue 11, 2017, Pages 1147-1153, ISSN 0168-8510

[12] World Bank. {2019}. {Air Quality Management – Poland, Final Report Report No: AUS0000585 Poland}. © World Bank.

[13] Nuclear Energy Agency, The Financing of Nuclear Power Plants, OECD 2009, NES No. 6360, Organization for Economic Co-operation and Development

[14] IPCC, 2014: Climate Change 2014: Synthesis Report. Contribution of Working Groups I, II and III to the Fifth Assessment Report of the Intergovernmental Panel on Climate Change [Core Writing Team, R.K. Pachauri and L.A. Meyer (eds.)]. IPCC, Geneva, Switzerland, 151 pp.

[15] IEA (2023), CO_2 Emissions in 2022, IEA, Paris https://www.iea.org/reports/co2-emissions-in-2022, Licence: CC BY 4.0

Dinka Lale, Dubravko Pevec, Mario Matijević, An Economy Aspect of Different Nuclear Energy Development, Journal of Energy, vol. 74 Number 3 (2025), 12–16
https://doi.org/10.37798/2025743722

Journal of Energy

VOLUME 74 Number 3 | 2025

journal homepage: http://journalofenergy.com/

Benchmark Calculation of FHR Fuel Assembly Phase I-C Depletion Exercises

Radomir Ječmenica, Davor Grgić, Paulina Družijanić, Bojan Petrović

Summary — **This paper presents our initial results for the Fluoride-salt High-temperature Reactor (FHR) physics benchmark calculations in Phase I-C, focusing on depletion exercises 5 and 6. In this Phase, the model is extended from the previous OECD benchmarks (Phases I-A and I-B) by transitioning from a pseudo-2D to a full 3D representation of a single FHR fuel assembly featuring TRISO fuel, graphite moderator, and FLiBe coolant. The pseudo-2D geometry is extruded axially, incorporating top and bottom reflectors (FLiBe and graphite), with radial periodic and axial vacuum boundary conditions applied. The benchmark's challenging aspects, including the complex 2D geometry of the plate-type assembly with TRISO fuel, the double heterogeneity spectral calculation, and the use of novel materials (FLiBe coolant and europium as a burnable poison), necessitate the use of Monte Carlo methods. We used the Serpent 2 code (versions 2.1.32 and 2.2.1) with two versions of the ENDF/B library (VI.8 and VII.1). Exercises 5 and 6 subdivide the fuel assembly into 20 axial regions with distinct material temperatures, however the primary distinction between these two exercises is the inclusion of integral burnable absorbers (Eu-151 and Eu-153 oxides) in the latter. The paper presents the results for k_{eff}, recoverable energy per fission, fission density rate, and axial offset in selected burnup points up to the final burnup of 70 GWd/tU. Additionally, we assessed the impact of different cross-section libraries, xenon modeling (transient versus equilibrium), and the depletion step length on the benchmark results.**

Keywords — **Serpent 2, Monte Carlo depletion calculation, FHR Benchmark Phase I-C, europium burnable absorber**

I. Introduction

The Fluoride-salt-cooled High-temperature Reactor (FHR) is an advanced molten salt reactor designed for high operating temperatures at low pressures. It is fuelled with tristructural-isotropic (TRISO) spheres embedded in fuel plates ("planks") of hexagonal fuel elements and cooled with fluoride salt 2LiF-BeF_2 (FLiBe). Due to complex geometry and novelty materials, an evaluation of the applicability of the methodologies and methods used to simulate FHR core physics is needed. Therefore, a benchmark under the auspices of OECD-NEA has been established to assess state of the art modelling and simulation capabilities for FHR reactor type [1]. The benchmark is divided in several phases. In Phase I, a model of a single fuel assembly is analysed. Phase II encompasses a 3D full core model with depletion and Phase III deals with a 3D full core model with feedback and multicycle analysis. Phase I has three subphases: I-A and I-B which cover the pseudo 2D model without and with depletion, respectively [2], and Phase I-C where a 3D model of a single fuel assembly is analysed [3]. The results of simulations of the pseudo 2D fuel assembly (Phase I-A and Phase I-B) performed by different FHR benchmark participants are published in [4]. In our previous work, we analyzed the first four Phase I-C benchmark exercises [5].

In this paper, we present initial results for Phase I-C depletion exercises 5 and 6. These exercises advance the pseudo-2D model into a comprehensive 3D simulation of an FHR fuel assembly with TRISO fuel, graphite moderator, and FLiBe coolant. The model incorporates an axially extruded geometry with top and bottom reflectors (FLiBe and graphite) and applies radial periodic and axial vacuum boundary conditions. The combination of complex geometry, double heterogeneity, and the use of novel materials (FLiBe coolant and europium as a burnable poison) necessitate application of Monte Carlo methods. We decided to perform calculations using Serpent 2 Monte Carlo code (versions 2.1.32 and 2.2.1 in Windows environment) with the ENDF/B-VI.8 and ENDF/B-VII.1 libraries.

II-.Methodology

A. Serpent 2

Serpent [6] is a 3D continuous energy neutron and photon transport code that has been developed at the VTT Technical Research Centre of Finland since 2004. It may be used for a wide range of particle transport applications such as reactor modelling, group constants generation, radiation transport, fusion, etc. The physics model covers neutron, photon and coupled neutron-photon simulations. Cross sections are read from ACE format data libraries. The continuous-energy interaction data is obtained from evaluated nuclear data files without major approximations. Standard tallies in Serpent enable calculating flux, power and reaction rate distributions in geometry cells and materials, as well as regular structures, such as lattices and super-imposed meshes.

Corresponding author: Radomir Ječmenica

Radomir Ječmenica, Davor Grgić and Paulina Družijanić are with the University of Zagreb Faculty of Electrical Engineering and Computing, Zagreb, Croatia (emails: radomir.jecmenica@fer.hr; davor.grgic@fer.hr; paulina.druzijanic@fer.hr).

Bojan Petrović is with Georgia Institute of Technology, Nuclear and Radiological Engineering, Atlanta, GA, USA (email: bojan.petrovic@gatech.edu)

Radomir Ječmenica, Davor Grgić, Paulina Družijanić, Bojan Petrović, Benchmark Calculation of FHR Fuel Assembly Phase I-C Depletion Exercises, Journal of Energy, vol. 74 Number 3 (2025), 17–23
https://doi.org/10.37798/2025743725

B. FHR FUEL ELEMENT MODELLING

FHR is utilizing prismatic fuel assemblies with a hexagonal base divided into three diamond-shaped sections (120 degree rotational symmetry), each containing six fuel planks. The model is shown in Figure 1. The apothem of the fuel hexagon is 22.5 cm and the outer dimension side-to-side is 45.0 cm. FLiBe inter-assembly gap is 1.8 cm, and assembly pitch is 46.8 cm. Each fuel plank is composed of two fuel stripes. Fuel stripes are prismatic regions composed of graphite matrix filled with a cubic lattice of TRISO. In the X–Y plane of each fuel stripe, there are 210×4 TRISO spheres. The TRISO lattice pitch is 0.09266 cm. The cross-section of the fuel element is shown in Figure 2. A TRISO sphere contains 5 layers: fuel kernel, buffer, inner pyrolytic carbon, silicon carbide layer, and outer pyrolytic carbon. Axial distribution of TRISO particles is shown in Figure 3. The control rod is a Y-shape structure made of MHC (Molybdenum-Hafnium Carbide alloy) with no cladding, surrounded by a thin layer of FLiBe. Each control rod wing is 10 cm long and 1 cm thick.

The 3D model of the FHR fuel element was extruded from the pseudo-2D fuel element geometry in axial direction with addition of axial top and bottom reflectors (FLiBe and graphite). Radially, periodic boundary conditions (BC) were applied, and axially vacuum BCs were used (Figure 4).

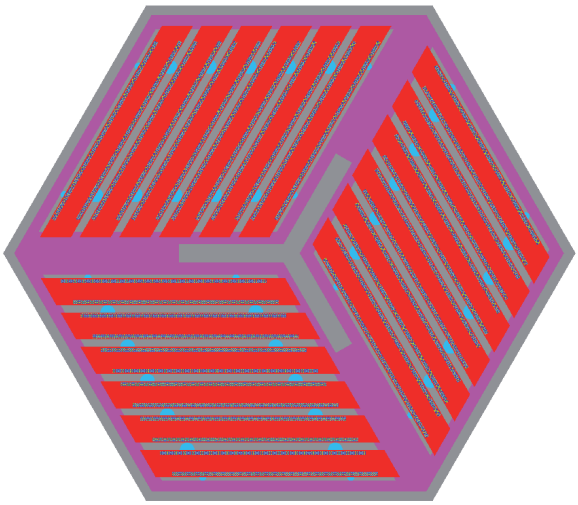

Fig. 1. FHR fuel assembly X-Y cross section in active fuel part

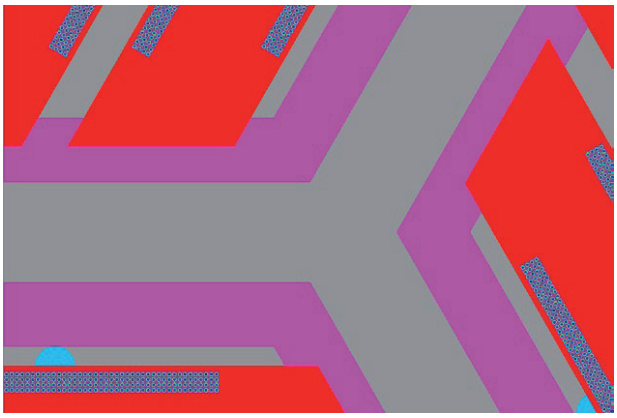

Fig. 2. FHR fuel assembly X-Y cross section in active fuel part zoomed to view TRISO spheres

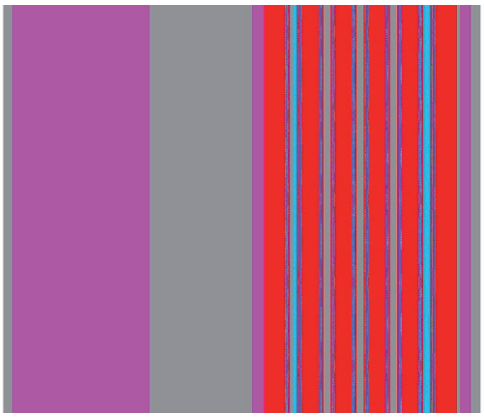

Fig. 3. Axial distribution of TRISO spheres

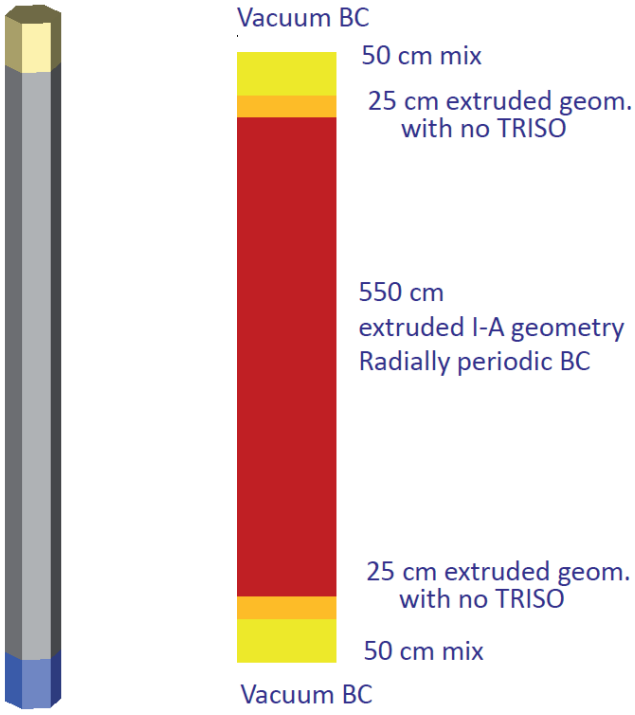

Fig. 4. FHR fuel assembly axial division and boundary conditions [3]

C. BENCHMARK EXERCISES

Phase I-C consists of 6 exercises. A summary of all Phase I-C exercises is given in Table 1. Exercises 1 - 4 were analysed in our previous work [5]. The first Phase I-C depletion exercise is Exercise 4. It assumes an axially symmetric core with uniform temperature and depletion is performed for a single axial fuel zone. Exercises 5 and 6 use a fuel assembly model consisting of 20 axial regions, bottom and top axial reflectors, bottom and top extruded geometry (the same as fuel region but without TRISO spheres), and 16 equidistant regions within active fuel. Axially, each region contains 371 TRISO spheres. These regions have different but fixed material temperatures (fuel kernel, graphite, and FliBe). The difference between Exercises 5 and 6 is in the presence of integral burnable absorbers (BA) in the latter case.

Burnable absorbers (in the form of Eu_2O_3) are contained in spheres with a radius of 0.035 cm. The axial distance between the centres of these spheres is 0.09266 cm, which means that each axial region contains 371 BA spheres. Axially, the centres of the

Radomir Ječmenica, Davor Grgić, Paulina Družijanić, Bojan Petrović, Benchmark Calculation of FHR Fuel Assembly Phase I-C Depletion Exercises, Journal of Energy, vol. 74 Number 3 (2025), 17–23
https://doi.org/10.37798/2025743725

TRISO spheres and the BA spheres coincide. In each of the 371 subregions within every plank, there are five BA spheres spaced 4 cm apart. Radially, the central BA sphere in each plank is positioned at half the width of the cooling channel.

The paper presents the results for k_{eff}, recoverable energy per fission, fission density rate, and axial offset in selected burnup points up to the final burnup of 70 GWd/tU. In addition to the influence of used cross-section libraries, we studied the influence of assumption on transient or equilibrium Xe during depletion and the length of integration step on the calculated results.

TABLE I
DESCRIPTION OF PHASE I-C EXERCISES

Exercises	Description
1	Axially symmetric core Uniform Axial Temperature, fuel kernel 1110 K, everything else 948 K
2	Reported vs actual convergence, the same as Exercise 1, but more spatial results requested
3	Control Rod insertion
4	Depletion as single region
5	Modified Exercise 4 with axial temperature distribution and fission density rate and depletion in 16 fuel zones
6	Modified Exercise 5 with discrete Eu poison present

The power density during depletion calculations was assumed constant at 200 W/gU. To satisfy the condition $\sigma_{k\text{-eff}} < 15 \cdot 10^{-5}$, 500 active generations with 50,000 neutrons per generation were used. A single burnup step under these conditions (Exercise 6) takes approximately three hours using ENDF/B-VII.1, and the program requires unreasonably long time (and large amount of memory) just to initiate the depletion calculation. For this reason, the calculations were performed first using the ENDF/B-VI.8 library. Planned comparison with SCALE burnup calculation results was cancelled because we used SCALE Windows version which does not have parallel capability and estimated running time was too long.

III. RESULTS

A. EXERCISE 5 RESULTS

The results of the Exercise 5 are k_{eff}, recoverable energy per fission, fission density rate, and axial offset calculated at selected burnup (BU) points up to the final burnup of 70 GWd/tU.

To illustrate the influence of the libraries used in the calculations, Figure 5 presents k_{eff} values during depletion for two different libraries, ENDF/B-VII.1 and ENDF/B-VI.8, while Figure 6 shows corresponding fission density rates axial distributions for Middle Of Cycle (MOC) and End Of Cycle (EOC). Figure 5 indicates that newer library gives lower k_{eff} values. The difference in effective multiplication factors is generally between 300 and 350 pcm, dropping below 150 pcm only at the initial burnup points. The choice of cross-section library has a non-negligible impact on the effective multiplication factor. Additionally, the cross-section library somehow affects the axial power distribution – not only in terms of Fission Density Rate (FDR) magnitudes but also in the sign of the axial offset. It is likely that at least AO differences are not just due to different libraries, but are due to a combination of library data, statistical uncertainty and the presence of Xe oscillations. A similar trend is observed in the axial power distribution at the end and at the middle of the cycle.

In Figure 7 axial offset as a function of burnup for equilibrium Xe and transient Xe calculation assumptions (22 BU points) is presented. As expected, the equilibrium xenon option results in lower absolute values of the axial offset during depletion.

Figure 8 presents the end-of-cycle axial distribution of U-235, Pu-239, and Xe-135 concentrations for different cross-section libraries and xenon calculation options. The U-235 concentration EOC axial distribution remains unaffected by the choice of cross-section library or xenon treatment during burnup (transient vs. equilibrium xenon). The impact of the cross-section library on Pu-239 concentration is relatively weak, whereas its effect on Xe-135 concentration is somewhat more pronounced. Xe calculation option has some influence on Xe distribution only.

Figure 9 presents the fission density rate for different numbers of burnup points (NEW: 22 points and FINE: 37 points) at 45, 50, and 65 GWd/tU. According to the Benchmark specifications, the obtained results should be provided at predefined burnup points. Depletion calculations were initially performed in 22 steps; however, unexpectedly early deviations in axial power distribution values were observed toward the end of the cycle, including changes in the sign of the axial offset. To address this, a depletion calculation was conducted using 37 burnup points (labelled as »FINE" in Figure 9), but the issue persisted, albeit to a lesser extent. The use of a newer cross-section library (ENDF/B-VII.1) might help resolve this issue, but equilibrium Xe calculation has inherent dependency on size of burnup step.

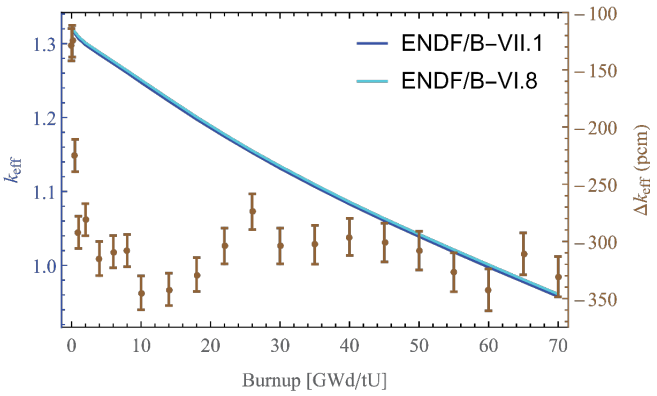

Fig. 5. k_{eff} during depletion for two cross section libraries

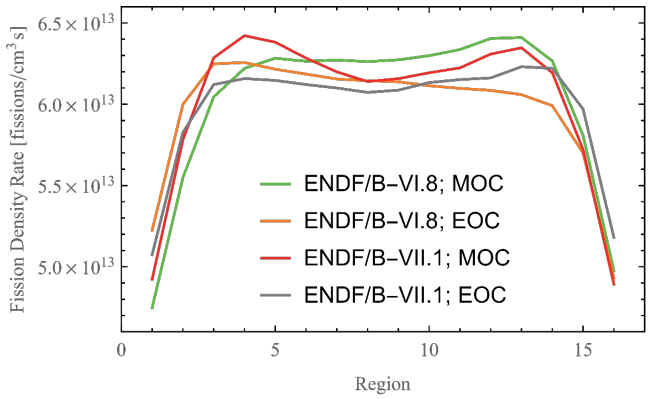

Fig. 6. Effect of the cross-section library on MOC and EOC axial distributions.

Radomir Ječmenica, Davor Grgić, Paulina Družijanić, Bojan Petrović, Benchmark Calculation of FHR Fuel Assembly Phase I-C Depletion Exercises, Journal of Energy, vol. 74 Number 3 (2025), 17–23
https://doi.org/10.37798/2025743725

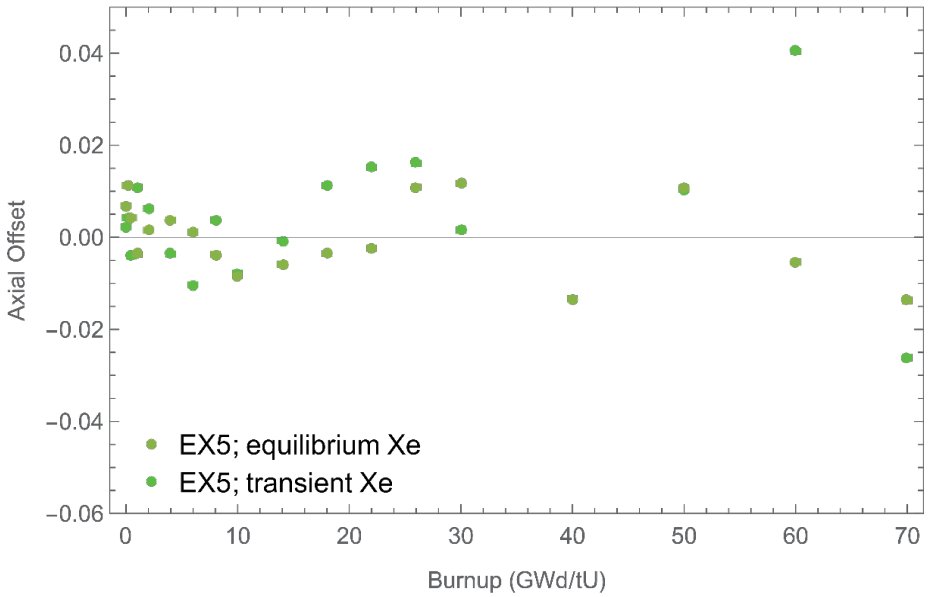

Fig. 7. Axial offset vs. burnup for equilibrium Xe and transient Xe calculation assumptions (22 BU points)

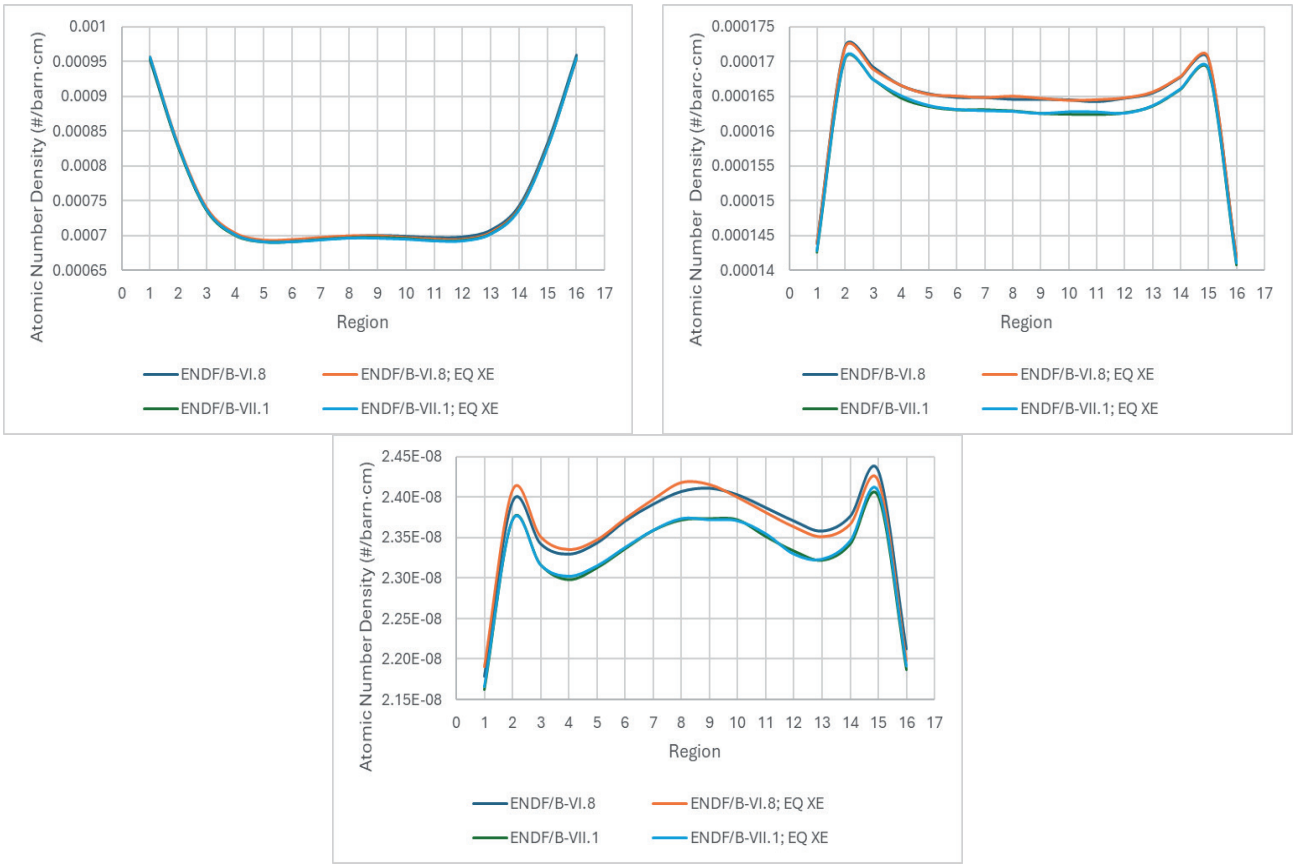

Fig. 8. EOC axial distribution of U-235, Pu-239 and Xe-135 concentration for different libraries and Xe calculation options

Radomir Ječmenica, Davor Grgić, Paulina Družijanić, Bojan Petrović, Benchmark Calculation of FHR Fuel Assembly Phase I-C Depletion Exercises, Journal of Energy, vol. 74 Number 3 (2025), 17–23
https://doi.org/10.37798/2025743725

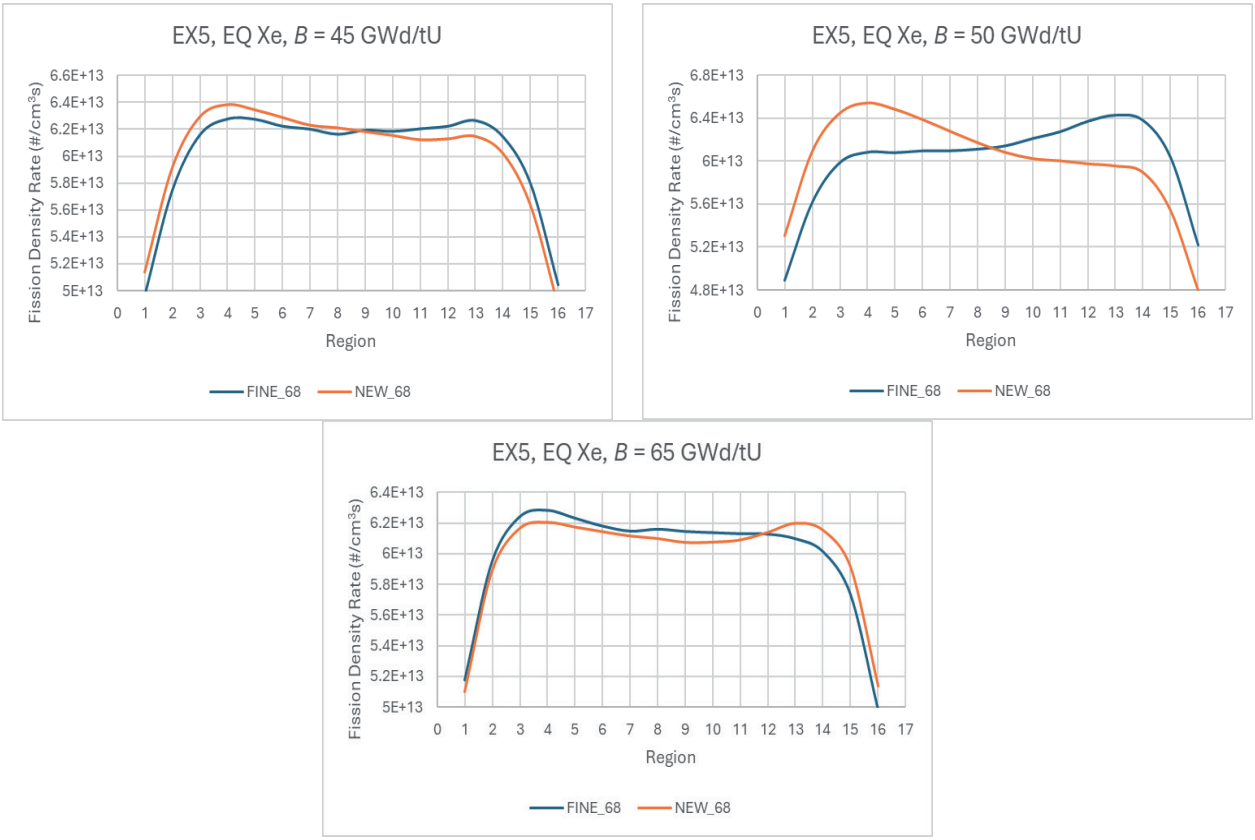

Fig. 9. Fission density rate for different number of depletion BU points (NEW 22 BU points, FINE 37 BU points) for 45, 50 and 65 GWd/tU

B. Exercise 6 results

The results of the Exercise 6 are k_{eff}, recoverable energy per fission, fission density rate, and axial offset calculated in selected burnup points up to the final burnup of 70 GWd/tU.

Figure 10 shows k_{eff} values for two cross-section libraries. At the beginning of depletion, the obtained k_{eff} values differ significantly – by up to 800 pcm. As the Eu-151 concentration decreases due to depletion, Δk_{eff} drops below 100 pcm. However, by the end of the cycle, it reaches approximately 400 pcm. Figure 10 clearly illustrates the significant impact of the cross-section library on $k_{eff}(B)$, the same as before the use of ENDF/B-VII.1 library results in lower k_{eff} values.

Figure 11 presents a comparison of the axial burnup distributions for Exercise 5 and Exercise 6 at MOC (30 GWd/tU) and EOC (70 GWd/tU). The impact of the cross-section library on the axial power distribution at MOC and EOC is not significant. In all considered cases, the obtained curves are smooth, with no obvious differences between them. Burnups obtained in exercise with integral burnup absorbers are typically higher in central part of the core.

Figure 12 shows the fission density rate axial distributions for BOC/MOC and EOC using two cross section libraries. Besides its magnitude, the differences are also evident in the shape of the FDR(z) curve, particularly in the sign of the axial offset. This effect is especially pronounced at the end of the cycle. As before, it is difficult to determine whether these differences are caused solely by library selection or by related statistical uncertainty and the presence of Xe instability.

Figure 13 presents the axial offset as a function of burnup for equilibrium Xe and transient Xe calculation assumptions (22 BU points). Based on Figure 13, it can be concluded that the equilibrium xenon option predominantly results in lower absolute values of the axial offset.

The EOC axial distribution of Eu-151 and Eu-153 concentrations for depletion with equilibrium and transient Xe is shown in Figure 14. Based on Figure 14, it can be concluded that different xenon treatments during depletion (transient vs. equilibrium Xe) have some impact only on the final concentration of the Eu-151 isotope, but not on the Eu-153 isotope.

Due to the burnable absorber presence and related spectral effects, the recoverable energy per fission values are consistently higher for Exercise 6 than for Exercise 5, as shown in Figure 15 for ENDF/B-VI.8 library and equilibrium Xe assumption used in calculation.

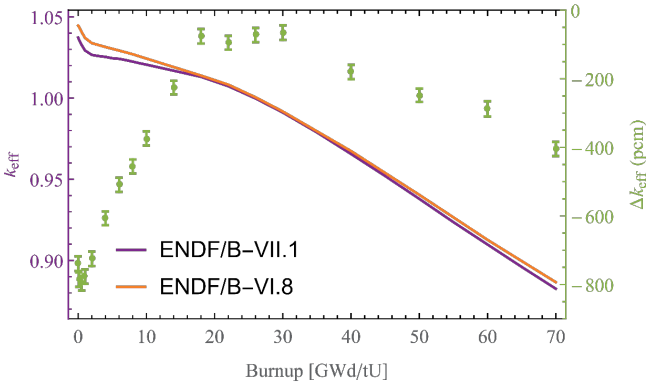

Fig. 10. k_{eff} during depletion for two cross section libraries

Radomir Ječmenica, Davor Grgić, Paulina Družijanić, Bojan Petrović, Benchmark Calculation of FHR Fuel Assembly Phase I-C Depletion Exercises, Journal of Energy, vol. 74 Number 3 (2025), 17–23
https://doi.org/10.37798/2025743725

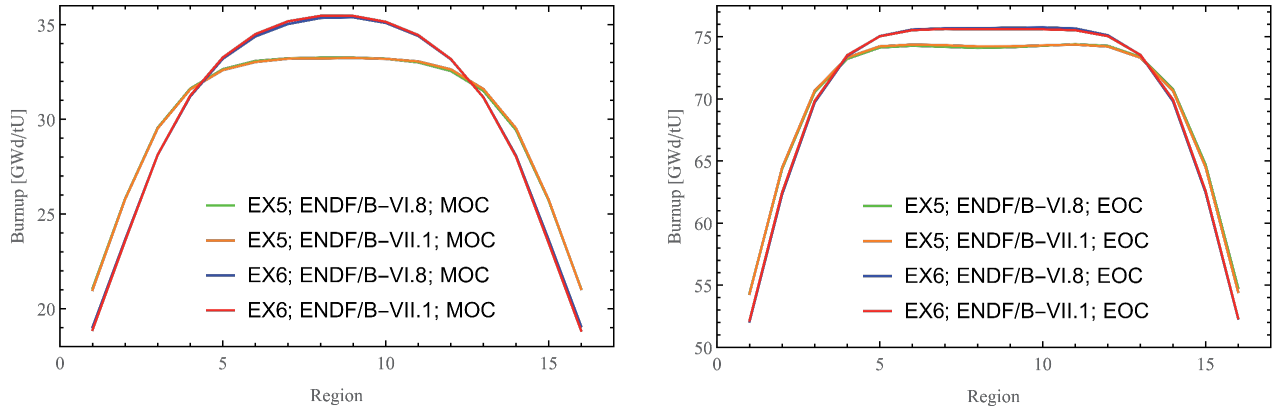

Fig. 11. Axial burnup distribution for MOC (30 GWd/tU) and EOC (70 GWd/tU), Exercise 5 and 6 (Eu as BA)

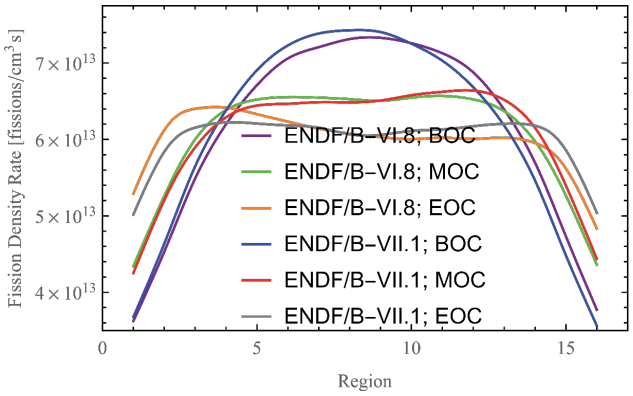

Fig. 12. The influence of used library on BOC, MOC and EOC axial distributions

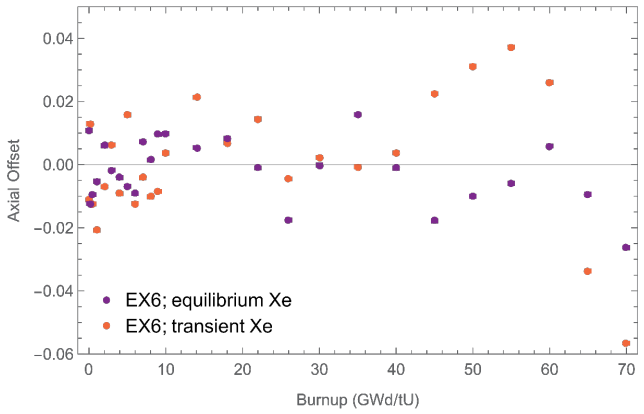

Fig. 13. Axial offset vs. burnup for equilibrium Xe and transient Xe calculation assumptions

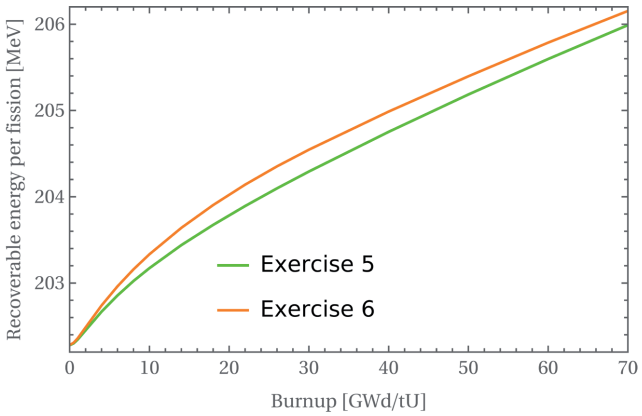

Fig. 15. Recoverable energy per fission as function of burnup, ENDF/B-VI.8, eq. Xe

IV. Conclusion

The initial results for Fluoride-salt High-temperature Reactor (FHR) reactor physics benchmark calculations, Phase I-C, depletion exercises 5, and 6 were presented. In addition to assessing the impact of the cross-section libraries used, we studied the influence of assumption on transient or equilibrium Xe treatment during depletion calculation and the length of depletion step on the calculated results. As expected, the choice of cross-section library significantly affects both k_{eff} and recoverable energy per fission. Some impacts are observed in the axial distributions of power and isotopic concentrations. Due to the nature of assumptions made during

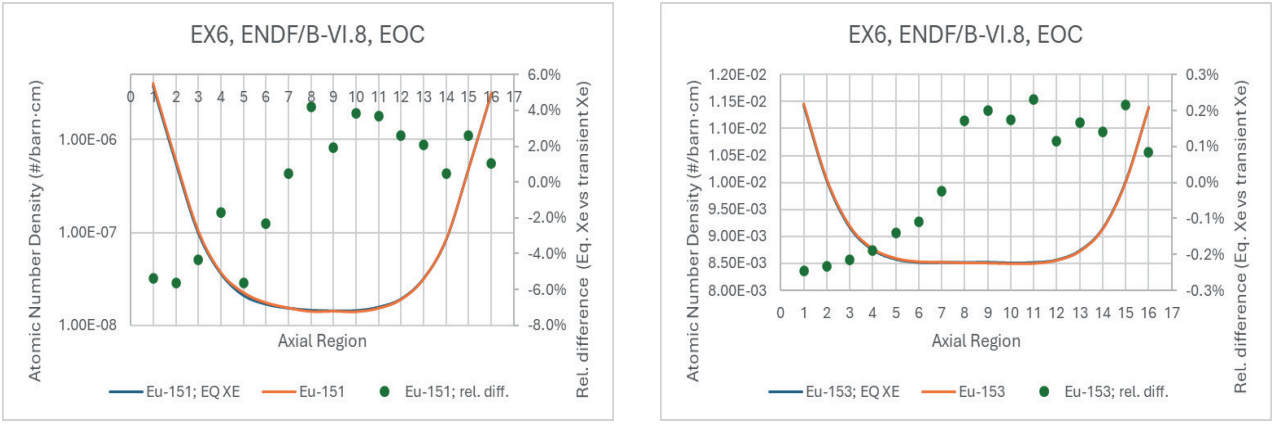

Fig. 14. EOC Eu-151 and Eu-153 concentration axial distribution for depletion with equilibrium and transient Xe

Radomir Ječmenica, Davor Grgić, Paulina Družijanić, Bojan Petrović, Benchmark Calculation of FHR Fuel Assembly Phase I-C Depletion Exercises, Journal of Energy, vol. 74 Number 3 (2025), 17–23
https://doi.org/10.37798/2025743725

depletion calculation, both length of burnup step and method used in the calculation of Xe concentration (equilibrium or full transient) have impact on the EOC axial power distributions. Therefore, more detailed guidelines (such as the number and the size of burnup steps or the assumption on Xe treatment) and more clear simulation requirements should be provided to be able to use each calculation tool specific capabilities and to simplify comparison of results between participants.

The Serpent 2 code has proven to be a good choice for this demanding modeling problem, considering aspects such as input preparation, code capabilities, and execution time. The selection of the cross section library is influencing both the obtained results and required computation time. Notably, a significant increase in calculation time and memory usage was observed during the preparatory phase of the Serpent 2 depletion calculations when switching from the ENDF/B-VI.8 to the ENDF/B-VII.1 library. Consequently, it is reasonable to perform all initial and sensitivity calculations using ENDF/B-VI.8 library and use ENDF/B-VII.1 library for the final calculations only.

References

[1] K. M. Ramey, B. Petrovic, "Monte Carlo modeling and simulations of AHTR fuel assembly to support V&V of FHR core physics methods", Annals of Nuclear Energy, 118 2018, pp. 272-282

[2] Benchmark Specifications for the Fluoride-salt High-temperature Reactor (FHR) Reactor Physics Calculations, NEA/NSC/R(2020)5, March 2021

[3] B. Petrovic, J. Faulkner, "Benchmark Specifications for the Fluoride-salt High-temperature Reactor (FHR) Reactor Physics Calculations Phase I-C: Fuel Element 3D Benchmark," in preparation, NEA Nuclear Science, OECD Publishing, Paris, France.

[4] K. M. Ramey et al., "Impact of molybdenum cross sections on FHR analysis", Nuclear Engineering and Technology, 54, 2022, pp. 817-825

[5] R. Ječemenica, D. Grgić, B. Petrović, P. Dučkić, Usage of Monte Carlo Code Serpent2 for Calculation of FHR Fuel Assembly, Proceeding of the International Conference Nuclear Energy for New Europe, 11-14 September 2023, Portorož, Slovenia

[6] J. Leppänen et al., »The Serpent Monte Carlo code: Status, development and applications in 2013.«Ann. Nucl. Energy, 82, 2015, pp. 142-150

Radomir Ječmenica, Davor Grgić, Paulina Družijanić, Bojan Petrović, Benchmark Calculation of FHR Fuel Assembly Phase I-C Depletion Exercises, Journal of Energy, vol. 74 Number 3 (2025), 17–23
https://doi.org/10.37798/2025743725

Journal of Energy
VOLUME 74 Number 3 | 2025
journal homepage: http://journalofenergy.com/

Verification of the IRIS Numerical Model for the Severe Accident Calculation

Siniša Šadek, Davor Grgić, Petra Strmečki, Zvonimir Čaić

***Summary* — The interest in the IRIS (International Reactor Innovative and Secure) reactor is revived by today's popularity of small modular reactors. The IRIS reactor project, led by Westinghouse Electric Corporation, was active in the first decade of the 21st century. Different groups of institutions such as nuclear manufacturers, academic institutions, national laboratories, etc. from 10 countries around the world participated in the IRIS team. IRIS is an integral, modular, medium sized (1000 MWt) pressurized water reactor. The IRIS reactor pressure vessel houses, beside the reactor core, also other major reactor coolant system components such as the pressurizer, reactor coolant pumps and steam generators. The lack of large pipes ensures high safety of the IRIS power plant and eliminates many causes of major accidents. This principle is known as "safety-by-design" approach. Polytechnic of Milan and the University of Zagreb were leading institutions in performing safety analyses for the IRIS reactor. The explicit coupling of RELAP5 and GOTHIC codes has been set up to cover the sequence of most probable LOCA transient events. This was necessary because the reactor vessel and the containment, once when the LOCA is initiated, become one hydraulic system with strong interaction. They exchange mass and energy which affects both systems in short time period and therefore cannot be treated separately as in a conservative analysis of a classic PWR nuclear power plant. In addition, the ASYST code model was recently developed to cover possible severe accident sequences. The core heat structures were replaced with SCDAP components to simulate core degradation. A couple of different GOTHIC models were developed to represent various arrangements of passive safety systems. A steady state analysis was performed to confirm the applicability of the IRIS numerical model in the safety analyses.**

***Keywords* — IRIS reactor, severe accident, RELAP5, GOTHIC, ASYST**

I. Introduction

IRIS (International Reactor Innovative and Secure) is an integral, medium power (1000 MWt), light water reactor [1], [2]. It is characterized by enhanced safety and improved economics. Although it features innovative and advanced engineering, it is based on the proven technology of pressurized water reactors (PWR). A "safety-by-design" approach is implemented in the IRIS system which objective is to prevent severe accidents from occurring rather than to mitigate their consequences. In order to enable such a strategy, all components of the reactor coolant system (RCS) are enclosed in a reactor vessel which eliminates large break loss-of-coolant accidents (LOCA) since there are no large piping or vessel penetrations. If the water leaks from the reactor vessel, the small containment will provide the necessary back-pressure to limit the loss of water, and in the later phase of the accident, the long-term cooling due to the innovative strategy of depressurization and retention of water inside the vessel.

Recently, there has been a considerable interest in small and medium sized modular reactors for many reasons: enhanced safety performance by using passive safety systems, the capability for flexible power generation, high availability, lower price comparing to larger units of nuclear power plants of second and third generations due to modular construction of several smaller units, etc. [3], [4]. Passive safety systems, such as the passive decay heat removal and the long-term gravity core cooling systems, used in the IRIS reactor are common in many small modular reactor (SMR) designs today, in a similar or slightly modified form [5], [6].

The IRIS reactor project, led by Westinghouse Electric Corporation, was active in the first decade of the 21st century. During the implementation of the project, 22 organizations from 10 countries participated in the IRIS team [7]. These organizations represented leading nuclear manufacturers, academic institutions, national laboratories and power producers, and covered different phases of the project (plant components design, licensing, testing, instrumentation and control, safety analyses, advanced cores, neutronics, source term, radioactive waste management, maintenance, utility perspective, etc.).

One of the more important activities of the IRIS project were the safety reactor analyses, coordinated by the Polytechnic of Milan and the University of Zagreb. As part of this activity, a preliminary safety assessment report (PSAR) was issued in 2003 [8]. A standard set of accidents was analyzed according to the requirements of the Chapter 15 of the Safety Analysis Report. In the section related to loss-of-coolant accidents resulting from a spectrum of postulated piping breaks within the reactor coolant pressure boundary, two failures were singled out as limiting LOCA events: double ended ruptures of a chemical volume and control system (CVCS) 4-inch pipe and the direct vessel injection (DVI) 2-inch pipe. The analyses have shown that the 10 CFR 50.46 acceptance criteria will not be exceeded for these small break (SB) LOCA scenarios.

Development of the IRIS numerical models for the codes RELAP5 [9], GOTHIC [10] and ASYST [11] is presented in the paper. The RELAP5 code is used for the analysis of the proce-

Corresponding author: Siniša Šadek

Siniša Šadek, Davor Grgić, Petra Strmečki and Zvonimir Čaić are with the University of Zagreb Faculty of Electrical Engineering and Computing, Zagreb, Croatia (emails: sinisa.sadek@fer.hr; davor.grgic@fer.hr; petra.strmecki@fer.hr, zvonimir.caic@fer.hr).

Siniša Šadek, Davor Grgić, Petra Strmečki, Zvonimir Čaić, Verification of the IRIS Numerical Model for the Severe Accident Calculation, Journal of Energy, vol. 74 Number 3 (2025), 24–29
https://doi.org/10.37798/2025743732

sses in the reactor vessel, the GOTHIC code for the analysis of the processes in the containment and the ASYST code for the severe accident calculation. RELAP5 and GOTHIC codes are explicitly coupled in order to correctly calculate mass and energy exchange between the reactor vessel and the containment [12]. A steady state analysis is performed, and the calculations of CVCS and DVI pipe breaks are repeated, in order to qualify the model at both levels: the steady state and the transient level.

II. IRIS SYSTEM DESIGN

IRIS consists of eight internal cooling loops. It has eight small, spool type, reactor coolant pumps and eight modular, helical coil, once through steam generators. The pressurizer is located in the reactor pressure vessel (RPV) upper head. The steel reflector surrounds the core and improves neutron economy, as well as it provides additional internal shielding. IRIS vessel is shown in Figure 1.

The steel containment of the IRIS reactor is spherical in shape, Figure 2, and

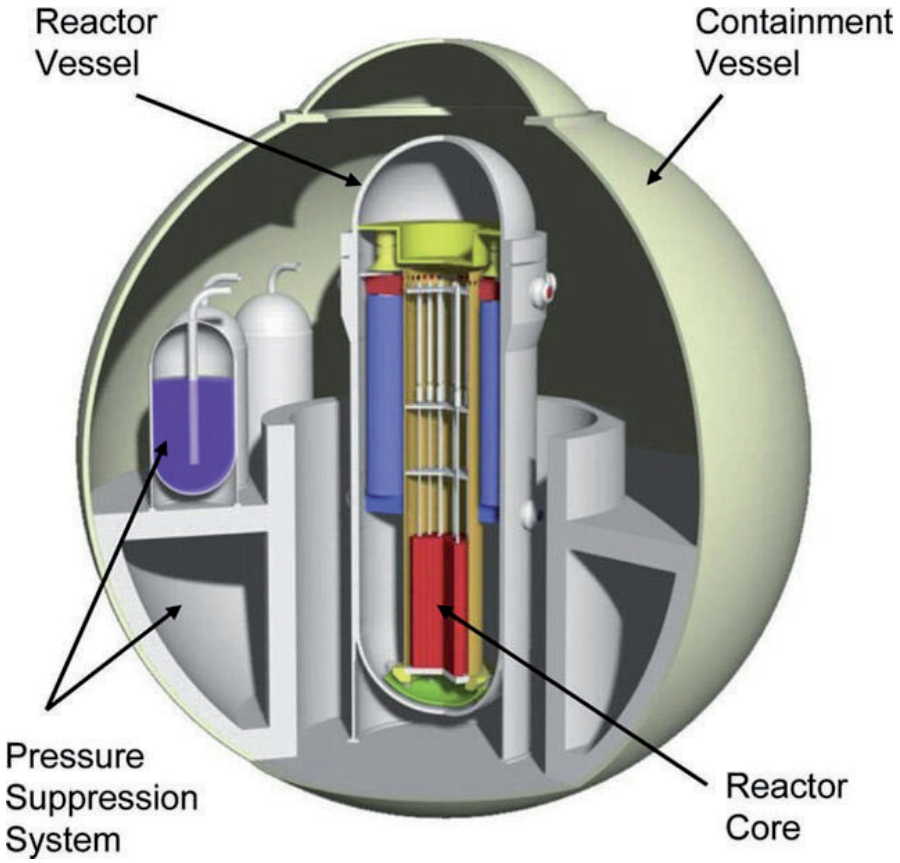

Fig. 2. Layout of the RPV and the containment

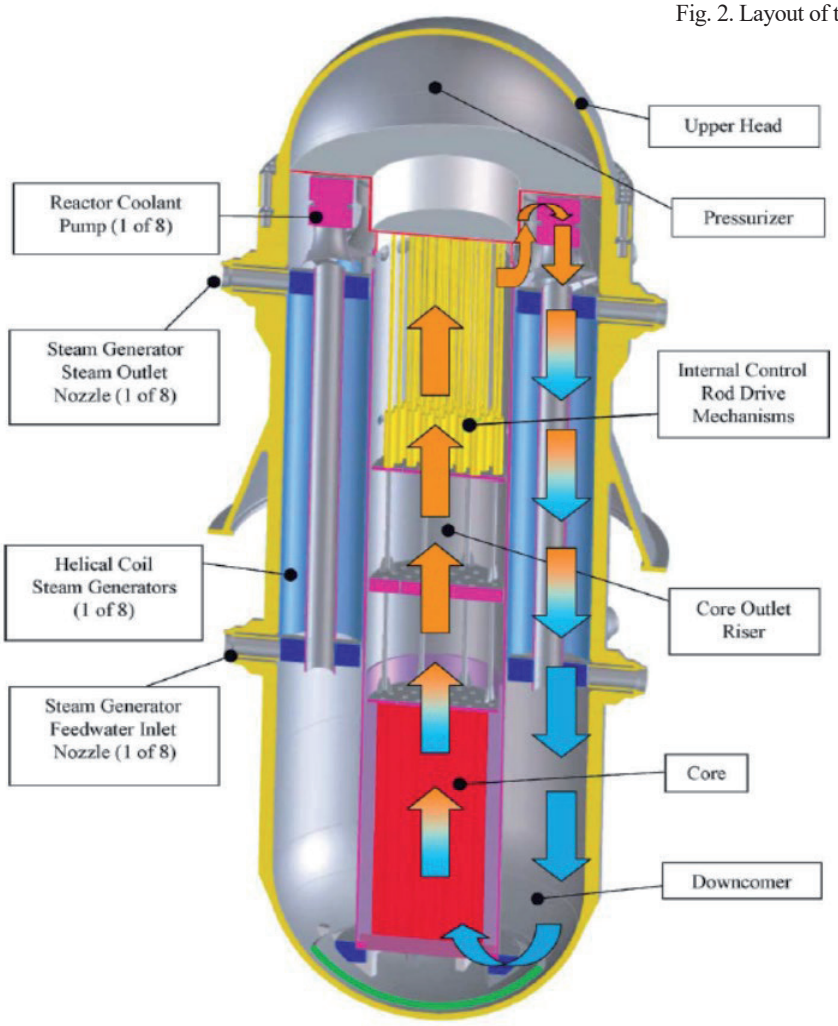

Fig. 1. Reactor pressure vessel of the IRIS reactor

relatively small in volume due to the integral design of the reactor vessel. Since the containment volume is reduced, compared to high power PWR power plants, its design pressure is high, 1.4 MPa. The automatic depressurization system (ADS), emergency boration tanks (EBT), pressure suppression pools, the long-term gravity make-up system (LGMS) and the associate pipelines, valves and other necessary supporting equipment are located inside the containment. The emergency heat removal system (EHRS) connection to feed and steam lines is made outside the containment, thus the refuelling water storage tank (RWST), containing EHRS heat exchangers, is also placed outside the containment.

Siniša Šadek, Davor Grgić, Petra Strmečki, Zvonimir Čaić, Verification of the IRIS Numerical Model for the Severe Accident Calculation, Journal of Energy, vol. 74 Number 3 (2025), 24–29
https://doi.org/10.37798/2025743732

III. Nodalization of the reactor vessel and the containment

A. Calculation models of primary and secondary systems

The RELAP5 nodalization is shown in Figure 3. The nodalization contains numerical models of reactor core flow channels, downcomer, lower plenum, core bypass, upper plenum, pressurizer, reactor coolant pumps, steam generators, emergency boration tanks, emergency heat removal system, ADS line, feedwater lines, steam lines and the DVI connections to LGMS tanks, reactor cavity and the pressure suppression system (PSS) tanks. The model also includes necessary reactor protection system functions for trips and their actuations.

The core structures: fuel rods, control rods, grid spacers and the core barrel are modelled with the ASYST code responsible for the simulation of a severe accident. Fuel assemblies are divided into four regions, Figure 4. The fuel assemblies in which the control rods are located are marked with an x. The radial division enables a more accurate temperature calculation that takes into account the differences in the fuel temperature in the centre and the periphery of the core. This temperature profile basically causes the central fuel assemblies to start melting before the assemblies in the outer core region. Each of the four ASYST fuel rod components is located in a separate RELAP5 thermal-hydraulic channel. The channels are interconnected by radial junctions to ensure lateral coolant flow in the event of a channel blockage due to core melting.

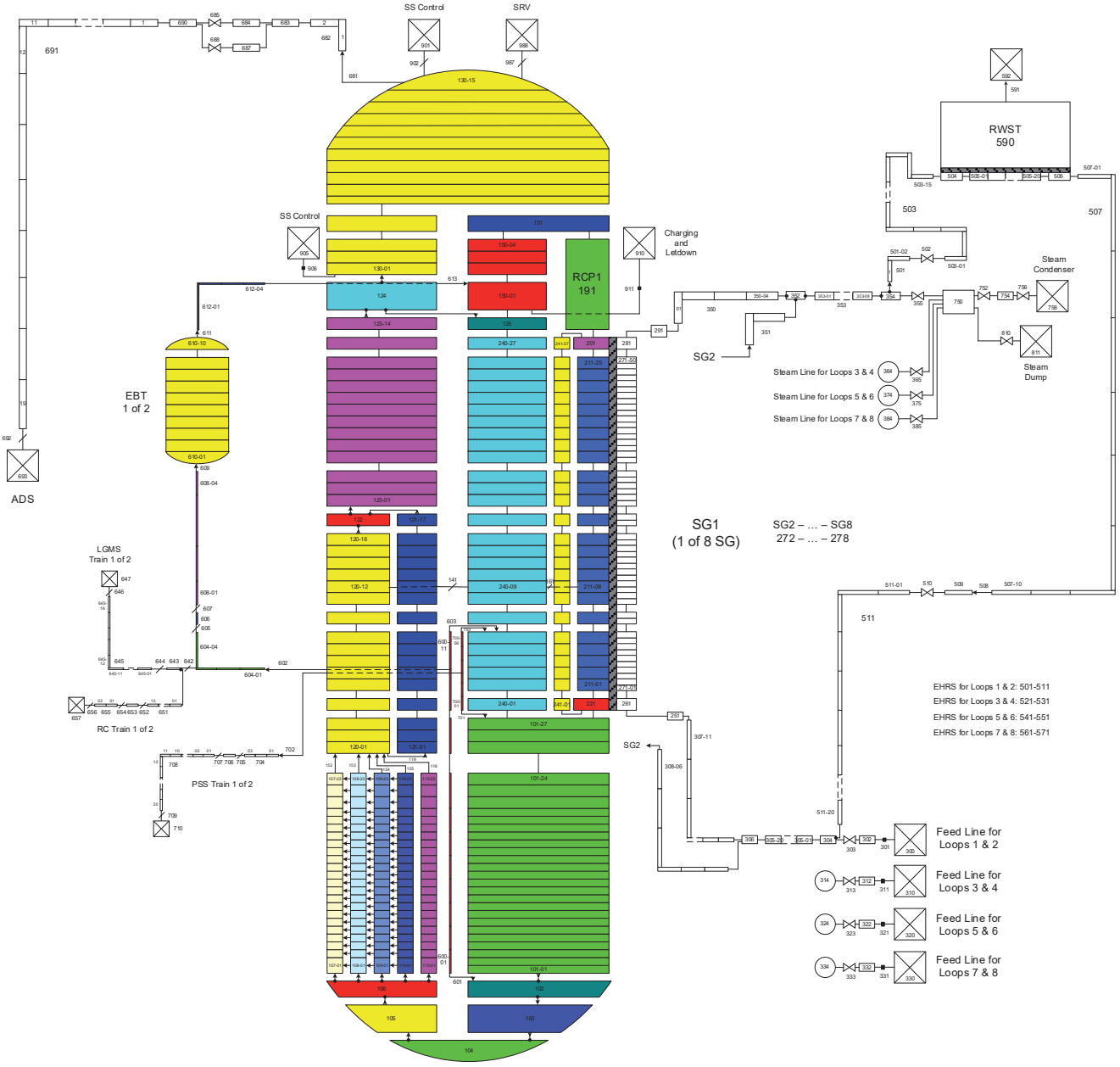

Fig. 3. RELAP5 nodalization

Siniša Šadek, Davor Grgić, Petra Strmečki, Zvonimir Čaić, Verification of the IRIS Numerical Model for the Severe Accident Calculation, Journal of Energy, vol. 74 Number 3 (2025), 24–29
https://doi.org/10.37798/2025743732

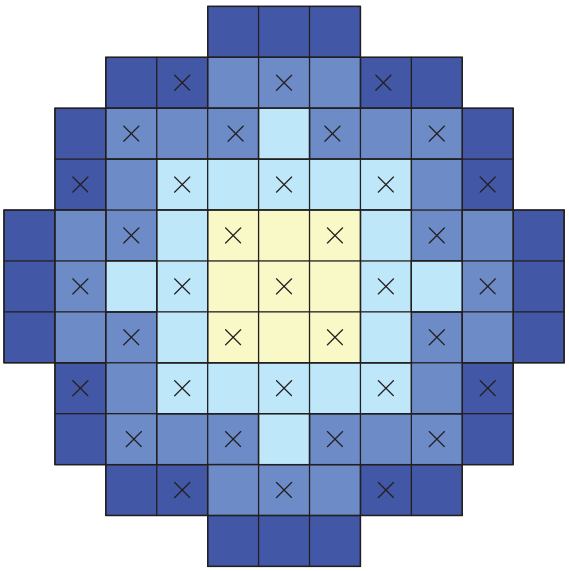

Fig. 4. Radial distribution of fuel assemblies inside the core

B. Containment models

The GOTHIC nodalizations of the containment are shown in figures 5 and 6. Nine control volumes and 15 flow paths are used in the original containment model, Figure 5. Drywell containment space is split in two parts (volumes 1 and 2) connected by the flow path 4. At the bottom, they are connected to the reactor cavity with two flow paths to simulate mixing between the volumes. Two LGMS tanks/suppression pools are connected to the air spaces (tanks) below them. Volumes 5 and 7 simulate vent pipes that connect the suppression pools to the containment atmosphere. The flow path 1 is used for break modelling. It connects reactor vessel with the cavity in which the coolant, released from the primary system, accumulates. Flow paths 8 and 9 are used to connect gravity make-up lines to the LGMS tanks. Flow paths 10 and 11 are used to connect gravity make-up lines to the reactor cavity. All those flow paths are connected to the DVI lines. The numbers at the other end of the lines represent RELAP5 time-dependent volumes, that is, boundary connections to the RELAP5 model.

The second nodalization which corresponds to the latest containment configuration is shown in Figure 6. The main difference to the old model is splitting of each of the two LGMS tanks/suppression pools in two separate water pools (4, 6, 8, 9). The suppression pools can also be connected by flow paths 25 and 26 to a separate direct vessel injection lines feeding water directly to the downcomer of the reactor vessel.

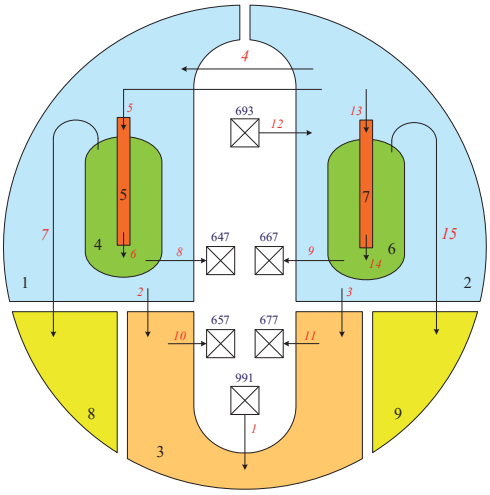

Fig. 5. GOTHIC containment nodalization for the older safety system configuration

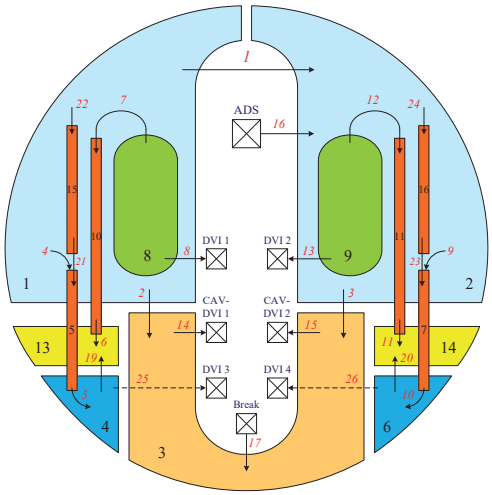

Fig. 6. GOTHIC containment nodalization for the newer safety system configuration

IV. Steady state calculation

In order to tune up the model and achieve correct initial conditions for the transient analysis, a steady state calculation for the reactor coolant system was performed with the RELAP5 code. The calculation simulated 2000 s of steady state operation with a time step of 0.05 s. Results are shown in Table 1. Comparison with the operational plant data shows that the model is qualified at the steady state level since the differences between the most important calculated parameters (pressurizer and SG pressures, reactor coolant and steam flow rates and temperatures, power transferred in steam generators) and reference values are less than 1%.

Table 1
Results of the Steady State Calculation

Parameter	Reference	RELAP5	Difference [%]
Pressurizer pressure [MPa]	15.5	15.512	0.08
Steam generator pressure [MPa]	5.8	5.784 – 5.809	–0.28 – 0.16
Core inlet temperature [K]	565.2	564.44	–0.13
Core outlet temperature [K]	603.15	602.18	–0.16
Reactor vessel mass flow [kg/s]	4707	4724	0.36
Core mass flow [kg/s]	4504	4524	0.44
SG steam exit temperature [K]	590.2	589.45 – 591.43	–0.13 – 0.21
Total steam flow [kg/s]	502.8	502.78	–0.004
Core pressure drop [kPa]	52.0	54.08	4.0
SG pressure drop [kPa] – primary	72.0	71.69	–0.43
SG pressure drop [kPa] – secondary	296.0	297.01	0.34
Total SG power [MW]	1002.0	1001.2	–0.08

Siniša Šadek, Davor Grgić, Petra Strmečki, Zvonimir Čaić, Verification of the IRIS Numerical Model for the Severe Accident Calculation, Journal of Energy, vol. 74 Number 3 (2025), 24–29
https://doi.org/10.37798/2025743732

V. Transient analysis

The calculations of the two limiting breaks at existing pipes are performed again with the intention of qualifying the numerical model at the transient level. The first break is the complete rupture of a CVCS 4-inch pipe, connected to the upper annular pump suction plenum of the reactor vessel. The second break is the double ended rupture of one DVI 2-inch pipe located in the lower annular region surrounding the steam generators.

The reactor coolant system pressure decreases due to the loss of coolant at the break and through the ADS, and due to heat removal by the EHRS. Natural circulation is established between the core and the steam generators; the steam condenses on the steam generator tube surface. More heat is removed by the EHRS via the steam generators than is produced in the core. Thus, the core temperature is decreasing. While the RCS pressure is decreasing, the pressure in the containment is increasing. When the containment pressure becomes greater than the pressure in the DVI lines, the safety injection from the long-term gravity make-up system tanks is activated.

The pressure inside the reactor pressure vessel decreases faster for the CVCS line break (Figure 7) because that pipe has a larger diameter than the DVI pipe, so more fluid is lost from the RPV to the containment. At 2500 s for the DVI pipe break, the reactor coolant system pressure decreases below the containment pressure and the higher pressure in the suppression pool gas space forces water to the reactor coolant system through the intact make-up line from the LGMS tank to the reactor vessel. There is no injection from the LGMS tank in the case of the CVCS line break. Water injection from the emergency boration tanks compensates for water loss through the break. In the case of a CVCS pipe break the collapsed core water level is higher than in the case of a DVI pipe break (Figure 8). This is because the water from the emergency boration tank connected to the damaged DVI pipe is directly discharged into the containment, which means that only one EBT is available, compared to the first case where both tanks are available. Both cases are design basis events since the acceptance criterion for the LOCA accident is met: the calculated maximum fuel rod cladding temperature is well below the threshold value of 1477 K (Figure 9) as defined by 10 CFR 50.46 LOCA regulations.

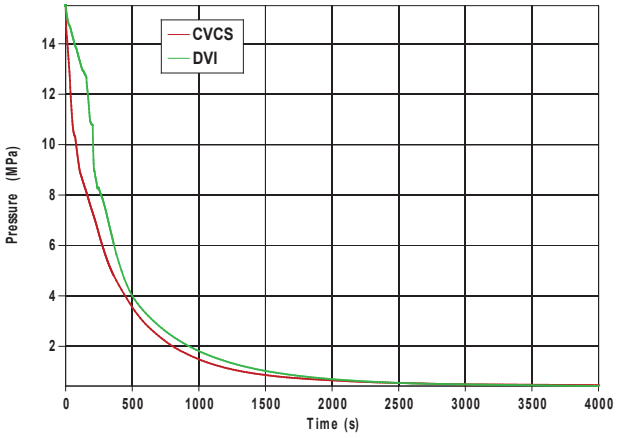

Fig. 7. Pressurizer pressure

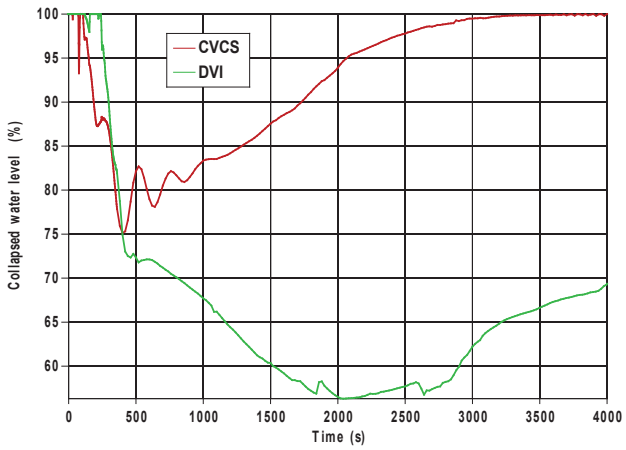

Fig. 8. Collapsed core water level

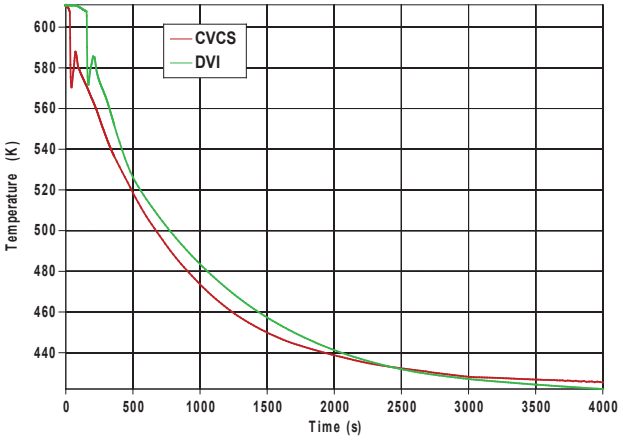

Fig. 9. Maximum fuel rod cladding temperature

VI. Conclusion

The best-estimate computer codes are needed for comprehensive safety analyses of complex thermal-hydraulic systems such as IRIS. The physical processes of natural circulation, core water level tracking, thermal-hydraulic coupling of the reactor vessel and the containment are correctly analyzed only if detailed nodalizations of reactor coolant system and containment are used. The transient calculations of CVCS and DVI pipe breaks show that overheating of the core and more serious consequences will not occur with proper operation of passive safety systems. The injection of borated water from the emergency boration tanks is a sufficient measure to control thermal-hydraulic conditions in the reactor vessel in the case of rupture of existing pipelines. Injecting water from the containment tanks (LGMS tanks, PSS pools) is a secondary safety measure since the main intention of the IRIS design is to maintain reactor coolant system inventory in the case of a design basis accident, rather than to rely on water injection from the external systems.

Acknowledgement

We gratefully express our appreciation to Dr. Chris Allison from Innovative Systems Software for his support and long-lasting cooperation in many research fields, including the use of RELAP5/SCDAPSIM and ASYST computer codes.

The work was carried out as part of the project HRZZ-IP-2024-05-4011 of the Croatian Science Foundation.

Siniša Šadek, Davor Grgić, Petra Strmečki, Zvonimir Čaić, Verification of the IRIS Numerical Model for the Severe Accident Calculation, Journal of Energy, vol. 74 Number 3 (2025), 24–29
https://doi.org/10.37798/2025743732

References

[1] Carelli, M.D., Conway, L.E., Oriani, L., Petrović, B., Lombardi, C.V., Ricotti, M.E., Barroso, A.C.O., Collado, J.M., Cinotti, L., Todreas, N.E., Grgić, D., Moraes, M.M., Boroughs, R.D., Ninokata, H., Ingersoll, D.T., Oriolo, F., 2004. The design and safety features of the IRIS reactor. Nucl. Eng. Des. 230(1–3), 151-167. https://doi.org/10.1016/j.nucengdes.2003.11.022.

[2] IRIS Plant Description Document, 2003. Westinghouse Non-Proprietary Class 3, WCAP-16062-NP, Westinghouse Electric Company LLC. https://www.nrc.gov/docs/ML0336/ML033600112.pdf.

[3] Ingersoll, D.T., 2009. Deliberately small reactors and the second nuclear era. Prog. Nucl. Energy 51 (4–5), 589-603. https://doi.org/10.1016/j.pnucene.2009.01.003.

[4] Reyes, Jr., J.N., Young, E., 2011. The NuScale Advanced Passive Safety Design. In: Proceedings of the ASME 2011 Small Modular Reactors Symposium, SMR2011-6658, 193-198. Washington, DC, USA. September 28–30, 2011. https://doi.org/10.1115/SMR2011-6658.

[5] Butt, H.N., Ilyas, M., Ahmad, M., Aydogan, F., 2016. Assessment of passive safety system of a Small Modular Reactor (SMR). Ann. Nucl. Energy 98, 191-199. https://doi.org/10.1016/j.anucene.2016.07.018.

[6] Marcel, C.P., Furci, H.F., Delmastro, D.F., Masson, V.P., 2013. Phenomenology involved in self-pressurized, natural circulation, low thermodynamic quality, nuclear reactors: The thermal–hydraulics of the CAREM-25 reactor. Nucl. Eng. Des. 254, 218-227. https://doi.org/10.1016/j.nucengdes.2012.09.005.

[7] Petrović, B., Carelli, M.D., Čavlina, N., 2006. IRIS – International Reactor Innovative and Secure: Progress in Development, Licensing and Deployment Activities. In: Proceedings of the 6th International Conference on Nuclear Option in Countries with Small and Medium Electricity Grids. Dubrovnik, Croatia, May 21-25, 2006.

[8] IRIS Preliminary Safety Assessment, 2003. Westinghouse Non-Proprietary Class 3, WCAP-16082-NP, Westinghouse Electric Company LLC. https://www.nrc.gov/docs/ML0322/ML032270062.pdf.

[9] RELAP5/Mod3.3 Code Manuals, 2001. Information Systems Laboratories, Inc., USA, NUREG/CR-5535, Prepared for U.S. Nuclear Regulatory Commission.

[10] GOTHIC Containment Analysis Package Manuals, 2005. Electric Power Research Institute, Version 7.2a, NAI 8907-02.

[10] ASYST VER 3 User Reference Manuals, 2020. SDTP/ADTP, Innovative Systems Software, Ammon, ID, USA.

[12] Grgić, D., Čavlina, N., Bajs, T., Oriani, L., Conway, L.E., 2004. Coupled RELAP5/GOTHIC model for IRIS SBLOCA analysis. In: Proceedings of the 5th International Conference on Nuclear Option in Countries with Small and Medium Electricity Grids. Dubrovnik, Croatia, May 16-20, 2004.

Siniša Šadek, Davor Grgić, Petra Strmečki, Zvonimir Čaić, Verification of the IRIS Numerical Model for the Severe Accident Calculation, Journal of Energy, vol. 74 Number 3 (2025), 24–29
https://doi.org/10.37798/2025743732

ENERGIJA